Research paper

Conservative semi-Lagrangian kinetic scheme coupled with implicit finite element field solver for multidimensional Vlasov Maxwell system

Hongtao Liu [a,b], Xiaofeng Cai [c], Giovanni Lapenta [b], Yong Cao [a,*]

[a] *School of Mechanical Engineering and Automation, Harbin Institute of Technology, Shenzhen 518055, China*
[b] *Department of Mathematics, Center for Mathematical Plasma Astrophysics, KU Leuven, University of Leuven, 3001, Belgium*
[c] *Research Center for Mathematics, Beijing Normal University at Zhuhai, and Division of Science and Technology, United International College (BNU-HKBU), Zhuhai, 519087, P.R. China*

ARTICLE INFO

ABSTRACT

In this paper, a conservative semi-Lagrangian (CSL) kinetic scheme coupled with an implicit finite element method (IFEM) is developed for multidimensional electromagnetic plasma simulations. The present method (CSL-IFEM) enjoys the respective advantages of the CSL and IFEM, including mass conservation, high-order spatial accuracy, as well as being free from the Courant-Friedrichs-Lewy (CFL) condition. In present CSL-IFEM, the CSL scheme with a general high order positivity-preserving limiter is utilized for the spatial discretization of the Vlasov equation, which enables the proposed method to remove the CFL limitation in phase space, exactly conserve mass, and preserve the positivity of the distribution function. The IFEM solver is developed for the spatial discretization of the Maxwell equation, which makes the current method free from CFL limitation induced by the speed of light and easily handles general field boundary conditions. To make the proposed CSL-IFEM more efficient in multidimensional simulations, the dimensional splitting procedure and sparse matrix technology are implemented in CSL and IFEM, respectively. Then the Vlasov solver CSL and Maxwell solver IFEM are coupled via the current density calculated from the general Ohm law. Finally, several numerical experiments, including electromagnetic wave (2d0v), particle gyromotion (0d2v), streaming Weibel instability (1d2v) and magnetic reconnection (2d3v), are performed to demonstrate the capabilities of the proposed method.

© 2021 Elsevier B.V. All rights reserved.

1. Introduction

Electromagnetic plasma has a large number of applications, including space propulsion, plasma sources for material processing, solar wind, magnetospheric and magnetically confined fusion devices [1]. Owing to the large variety of physical situations, the numerical simulation of plasma is still a great challenge for the scientific community. Roughly speaking, two large classes of physical models are available to describe plasma dynamic: fluid and kinetic models. The fluid models evolve

---

* Corresponding author.
E-mail addresses: liuhongtao@stu.hit.edu.cn (H. Liu), xfcai@udel.edu (X. Cai), giovanni.lapenta@kuleuven.be (G. Lapenta), yongc@hit.edu.cn, yongc@hitsz.edu.cn (Y. Cao).

macroscopic quantities depending on time and physical space, while kinetic models consider the time evolution of the microscopic distribution function which provides the probability of particles in a given state of phase space. It is well known that the fluid model is quite efficient, but will become less accurate once the continuum and thermodynamic equilibrium assumptions begin to break down [2]. Given the complex multi-scale characteristic of most plasma phenomena, the kinetic model is desired if a unified and accurate method for different regimes is required.

The basic kinetic model for electromagnetic plasma simulations is the Vlasov equation, coupled with the Maxwell equation. The numerical resolution of the Vlasov equation can mainly be classified into two categories: particle-based method and grid-based method. Particle in cell (PIC) is a well-known particle-based method based on tracing the motion of a finite number of macro-particles [3]. The biggest advantage of the PIC method is its computation economy, which is efficiently applied to high dimensional problems [4–9], but involves inherent numerical noise, especially for the plasma flow with small perturbations [10,11]. Alternatively, the grid-based method directly solves the kinetic equation in phase space, and has been widely used in nonequilibrium neutral flows [12–17]. We refer to this method as the direct kinetic method (DKM). As a deterministic method, the DKM is superior in reducing numerical noise and convenient to achieve high order accuracy for phase space discretization, which allows the study of fine-scale details that are inaccessible to PIC. In this paper, we aim to develop an accurate, stable and efficient DKM solver coupled with an implicit Maxwell solver for multidimensional multi-species electromagnetic plasma.

Various efficient and accurate DKM solvers have been proposed for the Vlasov equation, such as Eulerian or semi-Lagrangian finite difference [18–20], finite element [21–23], finite volume [24–28], and spectral methods [10,29,30]; see [31–33] for recent review of these methods. Among these kinetic solvers, we especially focus on the conservative semi-Lagrangian (CSL) scheme, since it not only can be free from the Courant–Friedrichs–Lewy (CFL) condition, but also exactly conserves mass. It is well known that mass conservation is important for an SL scheme, since non-conservation of mass might lead to instability of the scheme [34], especially in lengthy simulations [11]. In addition to the inherent conservative property, the positivity of the distribution function is another important property for Vlasov simulation, since the distribution function represents the probability of particles, which should not be negative. The non-positivity of the distribution function will induce some unphysical phenomenon [35] and further influence the stability of the scheme. Given the conservative form of the Vlasov equation, the multi-dimensional problems can be reduced to a succession of one-dimensional problems by dimensional splitting. With dimensional splitting, the multi-dimensional, including 5D and 6D, SL schemes have been developed for the Vlasov simulations [36–39]. Additionally, several interesting non-splitting schemes also have been proposed [40–42]. Among the SL schemes, the positive and flux conservative (PFC) method [24] is widely used in plasma simulations. Recently, Qiu et al. developed a general high order accurate SL Discontinuous Galerkin (DG) with maximum principle preserving (MPP) limiter [23] and SL WENO with parametrized MPP limiter [19] for Vlasov simulation, which provides a general way to design the desired accuracy and stable kinetic scheme.

In addition to the Vlasov solver, it is also crucial to develop a stable Maxwell solver for electromagnetic plasma simulations. Indeed, a vast array of possibilities exist in computational electromagnetism. It is well known that the traditional field solver involves the stability restriction, i.e., the numerical time step is limited by the CFL condition for the speed of light. To relieve this strict restriction, two methods are generally applied in plasma simulations: the Darwin approximation [38,43] and the implicit Maxwell solver [37,44]. Among the Maxwell solvers, we especially appreciate the implicit finite element method (IFEM) for its flexibility (easy to be applied to complicated geometry and various boundary conditions). To enclose the Vlasov-Maxwell (VM) system, the Vlasov solver and Maxwell solver should be coupled in an appropriate way. One popular way is the leapfrog scheme [37], where electromagnetic fields are advanced for a full time step but remain half a time step out of phase. An alternative way is to use the predictor-corrector scheme [45,46], where a second corrector is applied to the first-order predicted electric field using time-centered currents. Recently, the Hamiltonian splitting method is proposed for VM system [47]. Some high-order DG methods also have been applied in electromagnetic simulations [48,49]. However, most of the proposed direct kinetic solver for VM system has time step restriction induced either by Vlasov or by Maxwell equations. More recently, an energy-conserving implicit DG method has been developed for the VM system [50], but only in 1d2v single species plasma simulation. Hence it is necessary to design a more accurate, stable and efficient Vlasov Maxwell solver for multidimensional multi-species electromagnetic plasma simulation.

In this study, we present a third-order multidimensional electromagnetic plasma solver CSL-IFEM with the coupling of a positivity-preserving conservative semi-Lagrangian scheme and an implicit finite element field solver. More specifically, a third-order CSL scheme is implemented in the distribution function evolution, which enables the proposed method to remove the CFL limitation in phase space and exactly conserve mass. Combining with this CSL scheme, a general high order positivity-preserving limiter is utilized to preserve the positivity of the distribution function. To remove the CFL condition for speed of light and easily handle various field boundary conditions, a third-order IFEM is developed to update the electromagnetic field. Meanwhile, the different bases used in the test and trail function combined with numerical interpolation are designed to discretize the curl source term to make IFEM have uniformly third order accuracy in space. Then we bridge the CSL scheme and IFEM solver with the current density, which is obtained from the general Ohm law. Additionally, using the Strang splitting strategy in the CSL scheme and the Crank–Nicolson scheme in the IFEM solver ensures the proposed method to have second-order temporal accuracy, while using the dimensional splitting procedure in the CSL makes the proposed scheme more efficient in multidimensional plasma simulations. Finally, we present several multidimensional (from 2D to 5D) numerical experiments to demonstrate the accuracy, stability, and efficiency of the current method.

The rest of the paper is organized as follows. The VM system and its normalization are introduced in Section 2. In Section 3, the positivity-preserving CSL scheme, the third-order IFEM field solver, as well as the appropriate coupling of these two solvers for VM system are described in detail. We present the results of numerical studies in Section 4. Finally, a summary is given in Section 5.

2. The Vlasov-Maxwell system

In this section, we recall the nonrelativistic Vlasov-Maxwell system and present its normalization. The evolution of particles follows the Vlasov equation,

$$\partial_t f_s + \boldsymbol{v}_s \cdot \nabla_{\boldsymbol{x}} f_s + \frac{q_s}{m_s}(\boldsymbol{E} + \boldsymbol{v}_s \times \boldsymbol{B}) \cdot \nabla_{\boldsymbol{v}_s} f_s = 0, \tag{1}$$

where $f_s(\boldsymbol{x}, \boldsymbol{v}, t)$ is the velocity distribution function for species s moving in d_v-dimensional velocity space with $\boldsymbol{v}_s = (v_{s1}, \cdots, v_{sd_v})$ at position $\boldsymbol{x}$ and time t. Here q_s and m_s are the species charge and mass, while $\boldsymbol{E}$ and $\boldsymbol{B}$ are the electric field and magnetic field. The self-consistent electromagnetic fields $\boldsymbol{E}$ and $\boldsymbol{B}$ are generally given by the Maxwell equations,

$$\partial_t \boldsymbol{E} - c^2 \nabla \times \boldsymbol{B} = -c^2 \mu_0 \boldsymbol{J},$$
$$\partial_t \boldsymbol{B} + \nabla \times \boldsymbol{E} = 0, \tag{2}$$

where c is the speed of light, μ_0 is the vacuum permeability, and $\boldsymbol{J}$ is total current density. Besides, two constrains on electromagnetic fields are given by the Gauss law and the Thomson equation,

$$\nabla \cdot \boldsymbol{E} = \rho/\varepsilon_0, \quad \nabla \cdot \boldsymbol{B} = 0, \tag{3}$$

where ε_0 is the vacuum permittivity and ρ is the charge density. Note that the two constrains hold true for $t > 0$ as soon as they hold true at $t = 0$. However, that is not always true when the numerical approximations are considered. Some corrections [51–53] can be implemented to enforce the two constrains, which is beyond the scope of this paper.

In addition, it is well known that the Debye length λ and the electron plasma frequency ω_p are two important plasma parameters, which are given by

$$\lambda = \left(\frac{\varepsilon_0 k_B T}{q^2 n}\right)^{1/2}, \quad \omega_p = \left(\frac{nq^2}{\varepsilon_0 m_e}\right)^{1/2}.$$

where k_B is the Boltzmann constant, q is elementary charge, n is plasma number density, and T is plasma temperature.

To normalize the VM system, the following dimensionless variables are used:

$$\bar{x} = \frac{x}{x_0}, \bar{T} = \frac{T}{T_0}, \bar{m} = \frac{m}{m_0}, \bar{n} = \frac{n}{n_0}, \quad \bar{v} = \frac{v}{v_0},$$
$$\bar{t} = \frac{t}{t_0}, \bar{f} = \frac{f}{f_0}, \bar{\boldsymbol{J}} = \frac{\boldsymbol{J}}{J_0}, \bar{\boldsymbol{E}} = \frac{\boldsymbol{E}}{E_0}, \bar{\boldsymbol{B}} = \frac{\boldsymbol{B}}{B_0}, \tag{4}$$

where x_0, T_0, m_0, n_0, are reference length, temperature, mass, and number density, which are independent parameters. Then the reference velocity $v_0 = \sqrt{k_B T_0/m_0}$, time $t_0 = x_0/u_0$, distribution function $f_0 = n_0/v_0^{d_v}$, total current density $J_0 = q n_0 v_0$, electric filed $E_0 = k_B T_0/q x_0$, and magnetic field $B_0 = E_0/v_0$ can be further obtained. Once the four parameters x_0, T_0, m_0, n_0 are chosen, the dimensionless VM system will be uniquely determined.

In current study, we chose $T_0 = T_e$, $m_0 = m_e$, $n_0 = n_e$. The reference length x_0 will be given in the specific simulation. Define the dimensionless Debye length $\bar{\lambda} = \lambda/x_0$, and then the dimensionless electron plasma frequency is $\bar{\omega}_p = \omega_p t_0 = 1/\bar{\lambda}$. In the rest of this paper, all variables are dimensionless unless stated otherwise, but we will drop the bar over the variables for simplicity. Then the dimensionless VM system Eqs. (1) and (2) can be written as

$$\partial_t f_s + \boldsymbol{v}_s \cdot \nabla_{\boldsymbol{x}} f_s + \frac{q_s}{m_s}(\boldsymbol{E} + \boldsymbol{v}_s \times \boldsymbol{B}) \cdot \nabla_{\boldsymbol{v}_s} f_s = 0, \tag{5}$$

$$\lambda^2 \partial_t \boldsymbol{E} - \lambda^2 c^2 \nabla \times \boldsymbol{B} = -\boldsymbol{J},$$
$$\partial_t \boldsymbol{B} + \nabla \times \boldsymbol{E} = 0. \tag{6}$$

Note that the single-charged ion ($s = i$) or electron ($s = e$) is considered in the current paper, although the code allows arbitrary species. As a result, one can obtain $q_e = -1$, $q_i = 1$ from Eq. (5).

For the direct kinetic method, the key is to obtain the distribution function f_s. Once the distribution function f_s is known, the conservative variables $\boldsymbol{W}_s$ for species s can be obtained by

$$\boldsymbol{W}_s = (n_s, n_s \boldsymbol{u}_s, E_{ks})^{\mathrm{T}} = \int \boldsymbol{\psi} f_s d\boldsymbol{v}, \tag{7}$$

where $\boldsymbol{\psi} = (1, \boldsymbol{v}_s, v_s^2/2)^{\mathrm{T}}$ is the collision invariant, $\boldsymbol{u}_s$ is the plasma velocity, and E_{ks} is the kinetic energy. Then the charge density ρ_s and current density $\boldsymbol{J}_s$ for species s can be obtained from

$$(\rho_s, \boldsymbol{J}_s)^{\mathrm{T}} = q_s (n_s, n_s \boldsymbol{u}_s)^{\mathrm{T}}. \tag{8}$$

The total charge density ρ and current density $\boldsymbol{J}$ can be further given by

$$(\rho, \boldsymbol{J})^{\mathrm{T}} = \sum_s (\rho_s, \boldsymbol{J}_s)^{\mathrm{T}} . \tag{9}$$

For the traditional explicit Eulerian scheme, the numerical time step is determined by $\Delta t = \min(\Delta t_x, \Delta t_v, \Delta t_M)$, where $\Delta t_x = \mathrm{CFL}\Delta\boldsymbol{x}_{\min}/|\boldsymbol{v}|_{\max}$, $\Delta t_v = \mathrm{CFL}\Delta\boldsymbol{v}_{\min}/|\boldsymbol{a}|_{\max}$ with $\boldsymbol{a} = \frac{q_s}{m_s}(\boldsymbol{E} + \boldsymbol{v}_s \times \boldsymbol{B})$, and $\Delta t_M = \mathrm{CFL}\Delta\boldsymbol{x}_{\min}/c$ are the time step related to the transportation velocity $\boldsymbol{v}$ in Eq. (5), electromagnetic force $\boldsymbol{a}$ in Eq. (5), and the speed of light c in Eq. (6). Here $0 < \mathrm{CFL} < 1$ is the CFL number, $|\boldsymbol{v}|_{\max}$ and $|\boldsymbol{a}|_{\max}$ are the maximum transportation velocity and electromagnetic force, respectively, as well as $\Delta\boldsymbol{x}_{\min}$ and $\Delta\boldsymbol{v}_{\min}$ are minimum physical grid spacing and velocity grid spacing, respectively. With these CFL restrictions, the time step should be small enough to ensure the stability of the solver, especially the flows involved in the large transportation velocity, electromagnetic force, or the speed of light, which is not desired in the long-time simulation.

In the following section, we aim to develop a positivity-preserving conservative semi-Lagrangian scheme coupled with an implicit finite element field solver for VM system (5) and (6), where the numerical time step for the complete VM system is not restricted by the CFL condition related to transportation velocity, electromagnetic force and the speed of light.

3. Numerical methods

In this section, we will present a positivity-preserving and conservative semi-Lagrangian scheme coupled with a third-order implicit finite element field solver, termed CSL-IFEM, for VM system (5) and (6). The major steps of the proposed method include the update rule of the VM system, the CSL scheme for Vlasov equation, the IFEM solver for Maxwell equations, as well as the coupling of these two solvers.

3.1. Update rule

In order to solve the multi-dimensional VM system, we firstly split Vlasov Eq. (5) as follows,

$$\partial_t f_s + \boldsymbol{v}_s \cdot \nabla_{\boldsymbol{x}} f_s = 0 , \tag{10}$$

$$\partial_t f_s + \frac{q_s}{m_s}(\boldsymbol{E} + \boldsymbol{v}_s \times \boldsymbol{B}) \cdot \nabla_{\boldsymbol{v}_s} f_s = 0 . \tag{11}$$

Furthermore, the Eq. (5) can be achieved second order in time by solving Eq. (10) for a half time step, then solving Eq. (11) for a whole time step, followed by solving Eq. (10) for a second half time step, i.e., the Strang splitting. Specifically, the numerical update from $f_s^k(\boldsymbol{x}, \boldsymbol{v})$ (the solution at $t^k = k\Delta t$) to $f_s^{k+1}(\boldsymbol{x}, \boldsymbol{v})$ can be written in the form,

$$f_s^*(\boldsymbol{x}, \boldsymbol{v}) = f_s^k(\boldsymbol{x} - \boldsymbol{v}\Delta t/2, \boldsymbol{v}) , \tag{12}$$

$$f_s^{**}(\boldsymbol{x}, \boldsymbol{v}) = f_s^*\left(\boldsymbol{x}, \boldsymbol{v} - \frac{q_s}{m_s}\left(\boldsymbol{E}^{k+\theta} + \boldsymbol{v} \times \boldsymbol{B}^{k+\theta}\right)\Delta t\right) , \tag{13}$$

$$f_s^{k+1}(\boldsymbol{x}, \boldsymbol{v}) = f_s^{**}(\boldsymbol{x} - \boldsymbol{v}\Delta t/2, \boldsymbol{v}) . \tag{14}$$

It should be noted that Eqs. (12) and (14) represent the plasma transportation in physical space, which can be further solved exactly by the single splitting operators in each dimension. However, it is not the case for the plasma transportation in velocity space Eq. (13), since the splitting operators do not commute. To ensure second-order temporal accuracy for the whole system, the Strang splitting is again applied to Eq. (13). Certainly, some alternatives can be used [37,47,54]. Then the multi-dimensional Vlasov Eq. (5) is reduced to a succession of one-dimensional problems. This choice not only provides more alternative methods to solve the Eq. (5), but also makes the multi-dimensional simulation to be more practical.

On the other hand, the Maxwell equations (2) are discretized with the popular θ scheme (with $\frac{1}{2} \le \theta \le 1$),

$$\lambda^2 \frac{\boldsymbol{E}^{k+1} - \boldsymbol{E}^k}{\Delta t} - \lambda^2 c^2 \nabla \times \boldsymbol{B}^{k+\theta} = -\boldsymbol{J}^{k+1/2},$$
$$\frac{\boldsymbol{B}^{k+1} - \boldsymbol{B}^k}{\Delta t} + \nabla \times \boldsymbol{E}^{k+\theta} = 0 . \tag{15}$$

It is well known that Eq. (15) will have second-order temporal accuracy when $\theta = \frac{1}{2}$, which is the Crank–Nicolson scheme. Instead of solving $\boldsymbol{E}^{k+1}$ and $\boldsymbol{B}^{k+1}$ simultaneously, we utilize the relationship $\boldsymbol{u}^{k+\theta} = \theta\boldsymbol{u}^{k+1} + (1-\theta)\boldsymbol{u}^k$, where $\boldsymbol{u}$ denotes $\boldsymbol{E}$ or $\boldsymbol{B}$, and further rewrite Eq. (15) as the form that only contains the unknown electric field:

$$\lambda^2 \boldsymbol{E}^{k+\theta} + (\lambda c\theta\Delta t)^2 \nabla \times \nabla \times \boldsymbol{E}^{k+\theta} = \lambda^2 \boldsymbol{E}^k + \theta\Delta t\left(\lambda^2 c^2 \nabla \times \boldsymbol{B}^k - \boldsymbol{J}^{k+1/2}\right). \tag{16}$$

Analytically, the solution of Eq. (16) is equivalent to that of Eq. (15). But using Eq. (16) has some numerical advantages. It reduces the dimensions of the stiff matrix and makes the stiff matrix diagonally dominant [55,56], which definitely improves

the efficiency of the solver. If the electric field $\boldsymbol{E}^{k+\theta}$ is known, then the magnetic field can be obtained from the Faraday equation,

$$\boldsymbol{B}^{k+1} = \boldsymbol{B}^k - \Delta t \nabla \times \boldsymbol{E}^{k+\theta}. \tag{17}$$

Now, the key is to obtain the time evolution of the distribution function $f_s^{k+1}(\boldsymbol{x}, \boldsymbol{v})$, the electromagnetic field $\boldsymbol{E}^{k+\theta}$ and $\boldsymbol{B}^{k+\theta}$, as well as the current density $\boldsymbol{J}^{k+1/2}$.

3.2. Conservative semi-Lagrangian scheme

Note that the Eqs. (12), (13) and (14) with dimensional splitting can be further written is a unified form,

$$\partial_t f_s + \partial_x (a f_s) = 0, \tag{18}$$

where a denotes as velocity $\boldsymbol{v}$ in Eqs. (12) and (14), or Lorentz force $\frac{q_s}{m_s}(\boldsymbol{E}^{k+\theta} + \boldsymbol{v} \times \boldsymbol{B}^{k+\theta})$ in Eq. (13). The observation that Eq. (18) is the linear hyperbolic equation, which allows for the implementation of the conservative scheme following the characteristics lines. Here we employ the positive flux-conservative (PFC) scheme [24], which is briefly reviewed as follows:

Firstly, we introduce a set of mesh points $\{x_{i+1/2}\}_{I_i}$ of the computational domain $(x_{\min}, x_{\max})$, where $I_i = [x_{i-1/2}, x_{i+1/2}]$ are uniform numerical cells with centers $x_i = (x_{i-1/2} + x_{i+1/2})/2$ and cell sizes $\Delta x_i = x_{i+1/2} - x_{i-1/2}$. We use the $f_i^k = \frac{1}{\Delta x}\int_{x_{i-1/2}}^{x_{i+1/2}} f(x, t^k)dx$ to denote the cell averages of the solution over cell I_i. Tracking the characteristic lines of the cell $[x_{i-1/2}, x_{i+1/2}]$ backward, we can find its upstream cell $[x_{i-1/2} - a\Delta t, x_{i+1/2} - a\Delta t]$, which is denoted as $[x_{i-1/2}^*, x_{i+1/2}^*]$. Accordingly, we have

$$\int_{x_{i-1/2}}^{x_{i+1/2}} f(x, t^{k+1})dx = \int_{x_{i-1/2}^*}^{x_{i+1/2}^*} f(x, t^k)dx \,,$$

which can be further rewritten in the flux form,

$$f_i^{k+1} = f_i^k + F_{i-1/2} - F_{i+1/2} \,, \tag{19}$$

where $F_{i-1/2} = \frac{1}{\Delta x}\int_{x_{i-1/2} - a\Delta t}^{x_{i-1/2}} f^k dx$ and $F_{i+1/2} = \frac{1}{\Delta x}\int_{x_{i+1/2} - a\Delta t}^{x_{i+1/2}} f^k dx$.

Then we present the flux $F_{i+1/2}$ in the third order scheme in the case of $\varphi < 1$ and $a > 0$ [24],

$$F_{i+1/2} = \left(f_i^k + \frac{\varepsilon_i^+}{6}(2 - |\varphi|)(1 - |\varphi|)\left(f_{i+1}^k - f_i^k\right) + \frac{\varepsilon_i^-}{6}(1 - |\varphi|)(1 + |\varphi|)\left(f_i^k - f_{i-1}^k\right) \right)\varphi \,, \tag{20}$$

where $\varphi = a\Delta t/\Delta x$ is related to CFL condition, ε_i^+ and ε_i^- are the positivity-preserving limiter to ensure the positivity of the function f_i^{k+1}. Note that the case of $a \leq 0$ is mirror symmetric with respect to x_i of the above procedure, and for $\varphi \geq 1$, it can be handled with a whole grid shift followed by the cases of $\varphi < 1$. For preserving positivity, a specific flux limiter is used in the original PFC scheme [24],

$$\varepsilon_i^+ = \begin{cases} \min[1, 2f_i/(f_{i+1} - f_i)], & f_{i+1} - f_i > 0 \\ 1, & f_{i+1} - f_i \leq 0 \end{cases}$$

$$\varepsilon_i^- = \begin{cases} \min[1, -2f_i/(f_i - f_{i-1})], & f_i - f_{i-1} < 0 \\ 1, & f_i - f_{i-1} \geq 0 \end{cases}$$

It is nontrivial to apply the above limiter to a general high method. To achieve the uniform high order accuracy, we adopt a general high order parametrized positivity-preserving (PP) limiter in [19], which is designed as modifying the high order numerical flux towards the first order monotone flux in the following way

$$\hat{F}_{i+1/2} = \varepsilon_{i+1/2}\left(F_{i+1/2} - f_{i+1/2}\right) + f_{i+1/2} \,, \tag{21}$$

where $f_{i+1/2} = \varphi f_i^k$ is the first order flux, and $\varepsilon_{i+1/2} \in [0, 1]$. Note here $F_{i+1/2}$ is the high order flux obtained from Eq. (20) with $\varepsilon_i^+ = \varepsilon_i^- = 1$. Since the first order monotone flux have the property of positivity preserving [19], then we further have

$$\delta_i^k = -f_i^k + f_{i-1/2} - f_{i+1/2} \leq 0 \,.$$

To ensure the positivity of f_i^{k+1}, it is sufficient to have

$$\varepsilon_{i-1/2}\left(F_{i-1/2} - f_{i-1/2}\right) - \varepsilon_{i+1/2}\left(F_{i+1/2} - f_{i+1/2}\right) - \delta_i^k \geq 0$$

Let we denote $d_{i\pm 1/2} = F_{i\pm 1/2} - f_{i\pm 1/2}$ and $p_i = d_{i-1/2} - d_{i+1/2} - \delta_i^k$, the $\varepsilon_{i+1/2}$ can be given by the following formulas,

$$\varepsilon_i^l = \begin{cases} \min\left(1, \delta_i^k/d_{i-1/2}\right), & d_{i-1/2} < 0 \text{ and } d_{i+1/2} \leq 0, \\ \delta_i^k/\left(d_{i-1/2} - d_{i+1/2}\right), & d_{i-1/2}d_{i+1/2} < 0 \text{ and } p_i < 0, \\ 1, & \text{else} \end{cases}$$

$$\varepsilon_i^r = \begin{cases} \min\left(1, -\delta_i^k/d_{i+1/2}\right), & d_{i-1/2} \geq 0 \text{ and } d_{i+1/2} > 0, \\ \delta_i^k/\left(d_{i-1/2} - d_{i+1/2}\right), & d_{i-1/2}d_{i+1/2} < 0 \text{ and } p_i < 0, \\ 1, & \text{else} \end{cases}$$

where $\varepsilon_{i+1/2} = \min\left(\varepsilon_i^r, \varepsilon_{i+1}^l\right)$.

Finally, we employ the modified flux $\hat{F}_{i\pm1/2}$ to replace the flux $F_{i\pm1/2}$ in Eq. (19) to evolve the function f_i^{k+1},

$$f_i^{k+1} = f_i^k + \hat{F}_{i-1/2} - \hat{F}_{i+1/2} , \tag{22}$$

Thanks to the using of third PFC scheme [24] and the general high order PP limiter [19], the current CSL scheme is free from the CFL limitation, exactly preserve mass as well as the positivity of the distribution function with third spatial accuracy, which will be verified by the numerical test in Section 4.2.

3.3. Implicit finite element method

In this section, we utilize the implicit finite element method (IFEM) to solve Eq. (16), and define the electric field $\boldsymbol{E}$ and magnetic field $\boldsymbol{B}$ at cell nodes, while define the current density $\boldsymbol{J}$ at the cell center. To present the weak formulations of Eq. (16), we use $H^1(\Omega)$ to denote the usual Sobolev spaces, and use $(\cdot, \cdot)$ to denote L^2 inner product on domain Ω and $\langle \cdot, \cdot \rangle$ to denote L^2 inner product on the boundary $\partial\Omega$, e.g.,

$$(\boldsymbol{u}, v) = \int_\Omega \boldsymbol{u} \cdot v dV \text{ and } \langle \boldsymbol{u}, v \rangle = \int_{\partial\Omega} \boldsymbol{u} \cdot v ds .$$

Then the associated weak form of Eq. (16) can be written as the following system with the unknown $\boldsymbol{E} \in H^1(\Omega)$,

$$\left(\lambda^2 \boldsymbol{E}^{k+\theta}, \boldsymbol{\psi}\right) + \left(\lambda^2 \delta^2 \nabla \times \boldsymbol{E}^{k+\theta}, \nabla \times \boldsymbol{\psi}\right) = \left(\lambda^2 \boldsymbol{E}^k, \boldsymbol{\psi}\right) - \left(\delta/c\boldsymbol{J}^{k+1/2}, \boldsymbol{\psi}\right) + \left(\lambda^2 \delta c \nabla \times \boldsymbol{B}^k, \boldsymbol{\psi}\right) + \left\langle\lambda^2 \delta^2 \nabla \times \boldsymbol{E}^{k+\theta} \times \boldsymbol{n}, \boldsymbol{\psi}\right\rangle, \tag{23}$$

for any $\boldsymbol{\psi} \in H^1(\Omega)$, where $\delta = c\theta\Delta t$ and the Green formula $(\nabla \times \nabla \times \boldsymbol{E}, \boldsymbol{\psi}) = (\nabla \times \boldsymbol{E}, \nabla \times \boldsymbol{\psi}) - \langle\nabla \times \boldsymbol{E} \times \boldsymbol{n}, \boldsymbol{\psi}\rangle$ is used.

Then we introduce families of finite dimensional subspaces $\boldsymbol{E}_h \subset H^1(\Omega)$, $\boldsymbol{J}_h \subset H^1(\Omega)$ and $\bar{\boldsymbol{B}}_h \subset H^1(\Omega)$ to discretize Eq. (23). Choosing the set of basis functions $\{\boldsymbol{\psi}_i\}$ and $\{\bar{\boldsymbol{\psi}}_i\}$ span above subspaces, we can then approximate the electric field, current density and the curl of magnetic field as follows,

$$\boldsymbol{E} \approx \boldsymbol{E}_h = \sum_{i=1}^{N_1} \boldsymbol{E}_i(t)\boldsymbol{\psi}_i(x), \ \boldsymbol{J} \approx \boldsymbol{J}_h = \sum_{i=1}^{N_1} \boldsymbol{J}_i(t)\boldsymbol{\psi}_i(x), \ \nabla \times \boldsymbol{B} \approx \nabla \times \bar{\boldsymbol{B}}_h = \sum_{i=1}^{N_2} \bar{\boldsymbol{B}}_i(t)\nabla \times \bar{\boldsymbol{\psi}}_i(x) . \tag{24}$$

where N_1 or N_2 are global number of degrees of freedom. Plugging Eq. (24) into Eq. (23), one can obtain a linear system for $\boldsymbol{E}^{k+\theta}$, which can be further rewritten in the matrix form

$$\lambda^2 M \boldsymbol{E}^{k+\theta} + \lambda^2 \delta^2 M_d \boldsymbol{E}^{k+\theta} = \lambda^2 M \boldsymbol{E}^k - \delta/c M \boldsymbol{J}^{k+1/2} + \lambda^2 \delta c M_c \bar{\boldsymbol{B}}^k + F . \tag{25}$$

where the associated matrix is defined as

$$M = \left[\left(\boldsymbol{\psi}_i, \boldsymbol{\psi}_j\right)\right]_{i,j=1,\ldots,N_1}, \ M_d = \left[\left(\nabla \times \boldsymbol{\psi}_i, \nabla \times \boldsymbol{\psi}_j\right)\right]_{i,j=1,\ldots,N_1} ,$$

$$M_c = \left[\left(\boldsymbol{\psi}_i, \nabla \times \bar{\boldsymbol{\psi}}_j\right)\right]_{i=1,\ldots,N_1, j=1,\ldots,N_2} ,$$

$$F = \left[\left\langle\left(\lambda^2 \delta^2 \nabla \times \boldsymbol{E}^{k+\theta} \times \boldsymbol{n}\right)_i, \boldsymbol{\psi}_j\right\rangle\right]_{i,j=1,\ldots,N_1} .$$

A general matrix-assembling solver is used here to assemble the matrix in Eq. (25), where the solver is designed for a general integral with arbitrary partial derivative rather than a specific partial differential equation (PDE) [57,58]. More specifically, we first assemble each sub-matrix with a general matrix-assembling solver using the sparse matrix. Then we link each assembled sub-matrix by using a designed sparse tool to form the global matrix for expected PDE. Note the sparse tool we developed is similar to [59], which is used for the basic operations (e.g., the matrix addition, matrix-linking and so on) for the sparse matrix. In the present paper, the triangular elements with the classical Lagrange basis are used for simplification. Note that it is also possible to use some curl conforming finite element methods [44,60].

To achieve uniformly $l + 1$ order accuracy in space, the P^l Lagrange finite element basis function is used for all discretization in Eq. (25), except M_c which is related to the source curl term $(\nabla \times \boldsymbol{B}^k, \boldsymbol{\psi})$ in Eq. (23). More specifically, the different basis is used for trail function and test function in M_c (the source curl discretization): $\boldsymbol{\psi}_i$ (test fucntion) with P^l basis function while $\nabla \times \bar{\boldsymbol{\psi}}_j$ (trail function) with P^{l+1} basis function, where $i = 1, \ldots, N_1$ and $j = 1, \ldots, N_2$. On the other hand, in this paper, the basis $\boldsymbol{\psi}_i$ also will be used for the discretization of $\boldsymbol{B}$ in Eq. (17), i.e., $\boldsymbol{B} \approx \boldsymbol{B}_h = \sum_{i=1}^{N_1} \boldsymbol{B}_i(t)\boldsymbol{\psi}_i(x)$. Thus we need to reconstruct the unknown $[\bar{\boldsymbol{B}}_j^k]_{j=1,\ldots,N_2}$ from the known $[\boldsymbol{B}_i^k]_{i=1,\ldots,N_1}$, i.e., $\bar{\boldsymbol{B}}_j^k = \boldsymbol{I}\left(\boldsymbol{B}_i^k\right)$, where $\boldsymbol{I}$ is the interpolation operator. To obtained $\bar{\boldsymbol{B}}_j^k$ with expected order accuracy, two main steps are processed. First, we employ $l + 2$ order interpolation to obtain

unknown $\bar{\boldsymbol{B}}_j^k$ in each element e from given $\boldsymbol{B}_i^k$ in element e and its neighbors. Second, but importantly, we further employ the interpolation to update the $\bar{\boldsymbol{B}}_j^k$ for the nodes located at the edge of each element e from the $\bar{\boldsymbol{B}}_j^k$ for the inner nodes of element e and its neighbors, which strongly improve the stability. In this paper, $l = 2$ (third-order accurate scheme) is used, unless otherwise stated.

In order to obtain $\boldsymbol{E}^{k+\theta}$, the appropriate boundary condition should be applied in Eq. (25). Two popular boundary conditions in plasma simulation are taken into consideration in this paper: the perfect conductor boundary condition and the periodic boundary condition, which are denoted as Γ_c and Γ_p, respectively. The perfect conductor boundary condition, can be expressed as,

$$\boldsymbol{n} \times \boldsymbol{E}^{k+\theta} = 0, \ \ \lambda^2 \nabla \cdot \boldsymbol{E}^{k+\theta} = \rho^{k+\theta} \ , \tag{26}$$

where $\boldsymbol{n}$ is the normal vector of the boundary. With Eq. (26), we can derive $\nabla \times \boldsymbol{E}^{k+\theta} \times \boldsymbol{n} = 0$, which result in boundary integration $F = 0$. It should be noted that the second equation (Gauss law) is only calculated on Γ_c, which is necessary to close the whole linear system. Taking boundary at x direction for example, from $\boldsymbol{n} \times \boldsymbol{E}^{k+\theta} = 0$, we only can obtain $\boldsymbol{E}_y^{k+\theta} = 0$ and $\boldsymbol{E}_z^{k+\theta} = 0$, i.e., the Dirichlet boundary. Taking the Gauss law into consideration, the electric filed $\boldsymbol{E}_x^{k+\theta}$ can be determined by $\lambda^2 \nabla \boldsymbol{E}_x^{k+\theta} = \rho^{k+\theta}$, i.e., Neumann boundary condition. Similar treatment can be implemented on other boundary edges. Taking above constraints into Eq. (25) on Γ_c, $\boldsymbol{E}^{k+\theta}$ can be fully determined. Specially, in the quasi-neutral limit $\rho^{k+\theta} = 0$, we have $\lambda^2 \nabla \boldsymbol{E}_x^{k+\theta} = 0$ and would do nothing to enforce this boundary condition, since the zero Neumann boundary condition is naturally satisfied in IFEM.

In this paper, we apply the following constraints on the periodic boundary condition on Γ_p,

$$\boldsymbol{E}_i^{k+\theta} = \boldsymbol{E}_j^{k+\theta}, \ \ \nabla \boldsymbol{E}_i^{k+\theta} \cdot \boldsymbol{n} = \nabla \boldsymbol{E}_j^{k+\theta} \cdot \boldsymbol{n} \ , \tag{27}$$

where $\boldsymbol{E}_j^{k+\theta}$ undergoes periodic shift with respect to $\boldsymbol{E}_i^{k+\theta}$. The second constraint, i.e., the equality of normal gradient, is added to close the linear system. Additionally, we assume that tangential gradient of $\boldsymbol{E}_i^{k+\theta}$ and $\boldsymbol{E}_j^{k+\theta}$ are zero on Γ_p, which results in boundary integration $F = 0$. As a result, $\boldsymbol{E}^{k+\theta}$ can be further determined from Eq. (25) with the constraints of Eq. (27) on Γ_p. Here we use the GMRES iterative scheme [59] to solve the sparse linear system Eq. (25). In present work, we mainly focus on the efficiency and accuracy of the Maxwell solver. It is intersecting to extend the current IFEM to the conforming element, since the latter presents a possible method of completely avoiding divergence errors [44,60], which needs to be further investigated.

Once $\boldsymbol{E}^{k+\theta}$ is known, the magnetic $\boldsymbol{B}^{k+1}$ can be obtained in a similar way,

$$M\boldsymbol{B}^{k+1} = M\boldsymbol{B}^k - \Delta t M_c \bar{\boldsymbol{E}}^{k+\theta} \ , \tag{28}$$

where $\bar{\boldsymbol{E}}^{k+\theta} = \boldsymbol{I}\left(\boldsymbol{E}^{k+\theta}\right)$ with the similar treatment as $\bar{\boldsymbol{B}}^k$ in Eq. (25). Additionally, the Dirichlet boundary and periodic boundary condition should be implemented in Eq. (28). The periodic boundary condition is similar to Eq. (27), while the homogenous Dirichlet boundary $\boldsymbol{n} \cdot \boldsymbol{B}^{k+1} = 0$ is applied for perfect conductor boundary condition.

Accordingly, we can obtain the magnetic field $\boldsymbol{B}^{k+\theta}$,

$$\boldsymbol{B}^{k+\theta} = \theta \boldsymbol{B}^{k+1} + (1 - \theta)\boldsymbol{B}^k \ . \tag{29}$$

and the electric field $\boldsymbol{E}^{k+1}$,

$$\boldsymbol{E}^{k+1} = (\boldsymbol{E}^{k+\theta} - \boldsymbol{E}^k)/\theta + \boldsymbol{E}^k \tag{30}$$

Thanks to the using of P^2 element basis, the different basis for test and trial function combined with numerical interpolation in the source curl discretization, as well as the implicit temporal treatment, the present IFEM has third order spatial accuracy and removes CFL restriction induced by the speed of light, which can be verified by the numerical test in Section 4.1.

3.4. Coupling of CSL and IFEM

In this section we will present the process to evaluate the current density $\boldsymbol{J}^{k+1/2}$ and the way to couple CSL and IFEM. Taking the first moment of Vlasov Eq. (5), we find the following relation on the current density, which can be viewed as a generalized Ohm law [55],

$$\partial_t \boldsymbol{J} = \overline{\rho}\boldsymbol{E} + \bar{\boldsymbol{J}} \times \boldsymbol{B} - \nabla \cdot \overline{\boldsymbol{P}} \ , \tag{31}$$

where $(\bar{\rho}, \bar{\boldsymbol{J}})^{\mathrm{T}} = \frac{q_s}{m_s} \sum_s (\rho_s, \boldsymbol{J}_s)^{\mathrm{T}}$ and $\bar{\boldsymbol{P}} = q_s \sum_s \int \boldsymbol{v}\boldsymbol{v} f_s d\boldsymbol{v}_s$. With the Taylor expansion at time t^k, we can obtain that,

$$\boldsymbol{J}^{k+1/2} = \boldsymbol{J}^k - \frac{1}{2}\Delta t \nabla \cdot \bar{\boldsymbol{P}}^k + \frac{1}{2}\Delta t \left(\bar{\rho}^k \boldsymbol{E}^k + \bar{\boldsymbol{J}}^k \times \boldsymbol{B}^k\right). \tag{32}$$

Thanks to the evolution of Eq. (12), one can obtain that $\boldsymbol{J}_s^{k*} = \boldsymbol{J}_s^k - \frac{1}{2} q_s \Delta t \nabla \cdot \boldsymbol{P}_s^k$, where $\boldsymbol{J}_s^{k*} = \int q_s \boldsymbol{v}_s f_s^* d\boldsymbol{v}_s$. Note that Eq. (12) is equivalent to pre-update the position of the particle, which is similar to the PIC method [61] and avoids the computation of

the tensor $\boldsymbol{P}_s^k$. Then we can further rewrite Eq. (32) as follows,

$$\boldsymbol{J}^{k+1/2} = \boldsymbol{J}^{k*} + \frac{1}{2}\Delta t\left(\bar{\rho}^k\boldsymbol{E}^k + \bar{\boldsymbol{J}}^k \times \boldsymbol{B}^k\right), \tag{33}$$

where $\boldsymbol{J}^{k*} = \sum_s \int q_s\boldsymbol{v}_s f_s^* d\boldsymbol{v}_s$. Compared to Eq. (32), Eq. (33) avoids the computation of $\nabla \cdot \bar{\boldsymbol{P}}^k$ without any additional computational cost. As a result, we use Eq. (33) rather than Eq. (32) to evaluate $\boldsymbol{J}^{k+1/2}$. It should be noted that, to make the present method second order accurate in time, Eq. (12) and Eq. (14) can not be combined together in a more efficient way, since both $f_s^k(\boldsymbol{x}, \boldsymbol{v})$ and $f_s^*(\boldsymbol{x}, \boldsymbol{v})$ will be used in Eq. (33).

To provide a clearer understanding of proposed method and its implementation, here we present its evolution procedure. Starting from f_s^k, $\boldsymbol{E}^k$ and $\boldsymbol{B}^k$, the evolution procedure of proposed method from t^k to t^{k+1} can be described as follows:

(1) Calculate function f_s^* from f_s^k by solving Eq. (12) with Lie Splitting in physical space for $\Delta t/2$.
   (a) Compute the third order physical flux according to Eq. (20) in each physical direction;
   (b) Correct the physical flux with parametrized PP limiter by Eq. (21) in each physical direction;
   (c) Obtain function f_s^* Eq. (22) in each physical direction.
(2) Calculate the current density $\boldsymbol{J}^{k+1/2}$ by solving Eq. (33) for $\Delta t/2$, where $\boldsymbol{J}^{k*} = \sum_s \int q_s\boldsymbol{v}_s f_s^* d\boldsymbol{v}_s$.
(3) Update the Maxwell equations by IFEM for Δt.
   (a) Compute $\boldsymbol{E}^{k+\theta}$ by solving Eq. (25), where the calculation of the Maxwell source term and the treatment of boundary conditions refer to Section 3.3.
   (b) Update $\boldsymbol{B}^{k+1}$ according to Eq. (28).
   (c) Update $\boldsymbol{E}^{k+1}$ according to Eq. (30), and calculate $\boldsymbol{B}^{k+\theta}$ by solving Eq. (29).
(4) Update f_s^{**} by Eq. (13) with Strang Splitting in velocity space for Δt.
(5) Update f_s^{k+1} by Eq. (14) with Lie Splitting in physical space for $\Delta t/2$.

It should be noted that the process of step (4) and (5) in each dimension is similar to that of step (1), which are omitted for simplicity of presentation. Using the Strang splitting scheme for third spatial order CSL in Section 3.2 and the Crank–Nicolson scheme (with $\theta = \frac{1}{2}$) in IFEM in Section 3.3, as well as appropriate coupling CSL with IFEM Eq. (33) makes the proposed method second order accurate in time and third order accurate in space, which will be verified by the numerical test in Section 4.3. Using the sparse matrix in IFEM and the dimensional splitting in CSL makes the proposed method practical in 5D simulations, which will be verified by the numerical test in Section 4.4.

4. Numerical experiments

In this section, four numerical experiments, including electromagnetic wave (2d0v), particle gyromotion (0d2v), streaming Weibel instability(1d2v) and magnetic reconnection (2d3v), are implemented to validate the proposed CSL-IFEM. For sake of clarity, we state the specific version of the Vlasov-Maxwell system (5) and (6) used for each problem. Note that here we update the electromagnetic fields from Eq. (16) rather than Eq. (6). Transferring Eq. (6) to Eq. (16) is straightforward, we do not detail it. For all simulations, the periodic boundary conditions are considered for Eq. (13). The parameter θ is taken equal to 1/2 in IFEM solver.

To validate the accuracy of proposed CSL-IFEM, the L^2 error in space defined as

$$L_x^2(V) = \sqrt{\int\int |V(\boldsymbol{x}, \boldsymbol{v}) - V_r(\boldsymbol{x}, \boldsymbol{v})|^2 d\Omega}, \tag{34}$$

where V and V_r are the numerical results and reference results, respectively, and the volume $d\Omega$ depends on the specific simulation. Similarly, we define the L^2 error in time,

$$L_t^2(V) = \sqrt{\int |\hat{V}(t) - \hat{V}_r(t)|^2 dt}, \tag{35}$$

where $\hat{V}$ and $\hat{V}_r$ are the numerical results and reference results, respectively, which could be the space integration of V and V_r and will be defined in each specific question.

4.1. Electromagnetic wave

In this section, a 2d charge-free system electromagnetic wave is presented to validate the accuracy and efficiency (could use large time step) of proposed IFEM solver. More specifically, the transverse electric wave is considered here, where $\boldsymbol{E} = (E_x, E_y, 0)$ and $\boldsymbol{B} = (0, 0, B_z)$ are updated by,

$$\partial_t E_x - c^2 \partial_y B_z = 0,$$
$$\partial_t E_y + c^2 \partial_x B_z = 0,$$
$$\partial_t B_z + \partial_x E_y - \partial_y E_x = 0.$$

Table 1
Electromagnetic wave: $t = 1.0$, $\Delta t = (\Delta x/c)^{3/2}$. The L^2 error and convergence order in space.

V	$N = 16^2$		$N = 32^2$		$N = 64^2$		$N = 128^2$	
	L^2 error	Order	L^2 error	Order	L^2 error	Order	L^2 error	Order
E_x	1.23E-02	–	1.69E-03	2.86	2.14E-04	2.98	2.83E-05	2.92
E_y	1.27E-02	–	1.70E-03	2.91	2.11E-04	3.01	2.81E-05	2.91
B_z	1.12E-02	–	1.35E-03	3.05	1.81E-04	2.89	2.25E-05	3.01

Table 2
Electromagnetic wave: $t = 1.0$, $N = 64^2$. The L^2 error and convergence order in time.

V	CFL = 1		CFL = 2		CFL = 4		CFL = 8	
	L^2 error	Order	L^2 error	Order	L^2 error	Order	L^2 error	Order
E_x	1.36E-03	–	5.50E-03	1.97	2.21E-02	1.96	8.81E-02	1.87
E_y	1.37E-03	–	5.51E-03	2.00	2.22E-02	1.97	8.82E-02	1.87
B_z	2.21E-03	–	8.83E-03	1.99	3.46E-02	2.04	1.39E-01	2.12

In our simulations, the domain is set to be $[0, L_x] \times [0, L_y]$ with $L_x = 1$, $L_y = 1$ and is discretized with grids $N = N_x \times N_y$. The periodic boundary conditions are applied at $y = 0$ and $y = L_y$, while the perfect conductor boundary conditions are imposed at $x = 0$ and $x = L_x$. We initialize the electromagnetic field E_x, E_y, B_z at $t = 0$ following the analytical solutions [55],

$$E_x(t) = E_0 c k_y \cos(k_x x) \cos(k_y y) \sin(kct)/k_x ,$$
$$E_y(t) = E_0 c \sin(k_x x) \sin(k_y y) \sin(kct) ,$$
$$B_z(t) = E_0 k \cos(k_x x) \sin(k_y y) \cos(kct)/k_x ,$$

where $k_x = 2\pi/L_x$, $k_y = 2\pi/L_y$, $k^2 = k_x^2 + k_y^2$, $c = 1$ and $E_0 = 2$. Here we run this problem up to $t = 1$.

First, we test the spatial accuracy of the proposed IFEM. To ensure the spatial and temporal accuracy order is of the same order, here we set time step $\Delta t = (\Delta x/c)^{3/2}$. Table 1 shows the spatial L^2 error and convergence order of proposed IFEM with different physical grids N for the variable V, where V stands for E_x, E_y or B_z. Here L^2 error is evaluated with Eq. (34) for V, and V_r is the associated theoretical value. Third order convergence in space is clearly confirmed in Table 1. Note that the numerical experiments show that discretizing M_c in Eqs. (25) and (28) directly by the same basis (i.e., both $\boldsymbol{\psi}_i$ and $\nabla \times \boldsymbol{\psi}_j$ with P^2 basis function) only has second order accuracy in space. Thanks to the using of different basis combined with the numerical interpolation stated in Section 3.3, the present IFEM has uniformly third order convergence in space. This observation also holds with other boundary conditions (e.g., the full Dirichlet and full periodic boundary), but we don't present these results for brevity.

Then we investigate the temporal accuracy of the proposed IFEM. Here we let the time step $\Delta t = \text{CFL}/(\frac{c}{\Delta x} + \frac{c}{\Delta y})$, where CFL is the Courant-Friedrichs-Lewy number. Table 2 summaries the L^2 error and convergence order in time for different variables V with $N = 64^2$, where the error is evaluated in Eq. (35) with $\hat{V} = \sqrt{\int |V|^2 dxdy}$ and $\hat{V}_r$ is its associated theoretical value. Obviously, second order temporal accuracy is observed. Note that this observation only holds for $\theta = 1/2$, while first order accuracy would be observed for $\theta = 1$. Besides, taking different value of parameter $\theta > 1/2$ would introduce additional dissipation, where the electromagnetic energy will be damped. For more details, please refer to [55]. To make the scheme well preserve the energy and provide more accurate result, $\theta = 1/2$ is desired [6].

Thanks to the implicit θ scheme, the proposed IFEM could use a large CFL number as shown in Table 2. To more clearly show this argument, in Fig. 1 we plot the time evolution of electromagnetic energy with CFL = 0.5 and CFL = 5, where $E_{E_x} = \frac{1}{2}\int |E_x|^2 dxdy$ is the electric energy, $E_{B_z} = \frac{1}{2}\int |B_z|^2 dxdy$ is the magnetic energy, and $E_t = E_{E_x} + E_{E_y} + E_{B_z}$ is the total energy. Note that E_{E_y} is nearly equal to E_{E_x}, and we don't present it for brevity. As shown in Fig. 1, compared with the results using the small CFL number 0.5, despite of the small phase error, the present IFEM using the large CFL number 5 still predicts accurate results and conserves the total energy.

The above arguments indicate that the proposed IFEM has third order accuracy in space and second order accuracy in time (with $\theta = 1/2$), as well as being free from the CFL condition induced by the speed of light. In addition, all the simulations presented in this section are performed using the sparse matrix storage, which makes the proposed IFEM more practical in multidimensional simulations.

4.2. Particle gyromotion

In this section, the particle gyromotion (0d2v) [38,45] is presented to investigate the accuracy and efficiency of the proposed CSL. For simplification, the gyration of a positively charged particle in a fixed magnetic field $\boldsymbol{B} = (0, 0, B_z)$ in the velocity space $\boldsymbol{v} = (v_x, v_y, 0)$ is considered here. The particle follows

$$\partial_t f + (\boldsymbol{v} \times \boldsymbol{B})\nabla_{\boldsymbol{v}} f = 0$$
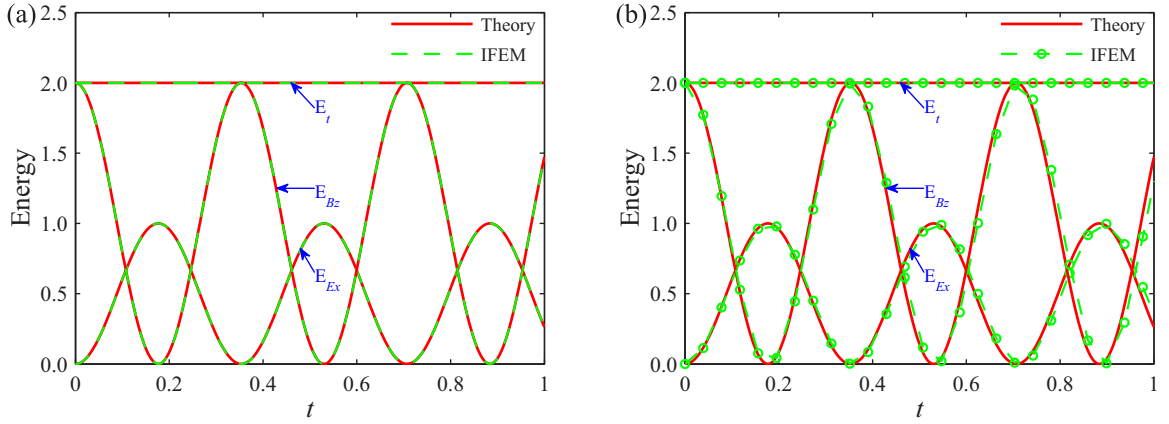
Fig. 1. Electromagnetic wave: $N_x = 64, N_y = 64$. The time evolution of electromagnetic energy with CFL = 0.5 (a) and CFL = 5 (b).

Table 3
Particle gyromotion: CFL = 1, $t = 2\pi$. The L^2 error and convergence order in space.

N	CSL-WO			CSL-WP		
	L^2 error	Order	f_{min}	L^2 error	Order	f_{min}
32^2	6.24E-02	–	−2.30E-03	6.03E-02	–	1.13E-21
64^2	1.18E-02	2.40	−1.02E-04	1.18E-02	2.35	3.54E-23
128^2	1.62E-03	2.86	−6.61E-10	1.62E-03	2.86	4.31E-27
256^2	2.07E-04	2.97	−1.87E-13	2.06E-04	2.98	1.33E-31

Table 4
Particle gyromotion: $N = 64^2, t = 2\pi$. The L^2 error and convergence order in time.

CFL	CSL-WO			CSL-WP		
	L^2 error	Order	f_{min}	L^2 error	Order	f_{min}
1	2.56E-04	–	−1.02E-04	3.04E-04	–	3.54E-23
2	1.02E-03	1.99	−3.87E-05	1.03E-03	1.59	1.29E-21
4	4.11E-03	2.01	−2.93E-06	4.11E-03	1.99	4.24E-23
8	1.65E-02	2.00	−4.64E-08	1.65E-02	2.00	3.31E-24

with the initial distribution function

$$f(v_x, v_y, 0) = \frac{1}{\pi} \exp[-(v_x - v_0)^2 - v_y^2].$$

In our simulation, the velocity space is set to be $[-v_{x_m}, v_{x_m}] \times [-v_{y_m}, v_{y_m}]$ with $v_{x_m} = v_{y_m} = 6$ and is discretized with grids $N = N_{v_x} \times N_{v_y}$. The fixed magnetic field $B_z = 1$ and drift velocity $v_0 = 1$. The time step is set to be $\Delta t = \text{CFL}\Delta v / a_{max}$ where $a_{max} = v_{x_m} B_z$.

First, we test the spatial accuracy of the proposed CSL scheme. Table 3 shows the spatial L^2 error and convergence order of the CSL with general parametrized PP limiter Eq. (21) (denoted by 'CSL-WP'), together with the results of CSL without the PP limiter (denoted by 'CSL-WO'). Here L^2 error is evaluated from Eq. (34) with $V = f$ and $V_r = f^0$, where f^0 is the function f at $t = 0$. In Table 3, the expected third order accuracy is observed. With the parametrized PP limiter, the numerical solutions of CSL-WP are strictly positive with $f_{min} \geq 0$, where f_{min} is the minimum numerical solution of CSL.

To investigate the temporal accuracy of proposed CSL, here we chose $\hat{V} = \int v_x f dv_x dv_y$ and $\hat{V}_r = \cos(t)$ for Eq. (35). Table 4 summaries temporal L^2 error and convergence order with $N = 64^2$. Second order accuracy in time and strictly positive with $f_{min} \geq 0$ for present CSL are clearly observed. The results in Table 3 and Table 4 shows that the PP limiter plays an important role in preserving the positivity in the simulation with low resolution and large iteration. For this simple case, both CSL-WO and CSL-WP are stable in lengthy time simulation and exactly conserve the mass, where the relative error is both about 10^{-13}. In this sense, it seems that it is not necessary to use the PP limiter. Unfortunately, the scheme which doesn't preserve positivity is not always as well behaved. More detail on the role of the positivity is presented in ref [19,23]. For this reason, in the remainder of the paper, the CSL is referred to CSL-WP, unless otherwise stated.

To further verify the capability of the present CSL, in Fig. 2 we plot the particle mean velocity phase plot expressed in u_x against with u_y over four gyro-periods ($t = 8\pi$), where $\boldsymbol{u} = \int \boldsymbol{v} f d\boldsymbol{v}$. The gyromotion of the particle is exactly captured even with large CFL = 15. Indeed, having the large time step is a big advantage of the semi-Lagrangian scheme, compared
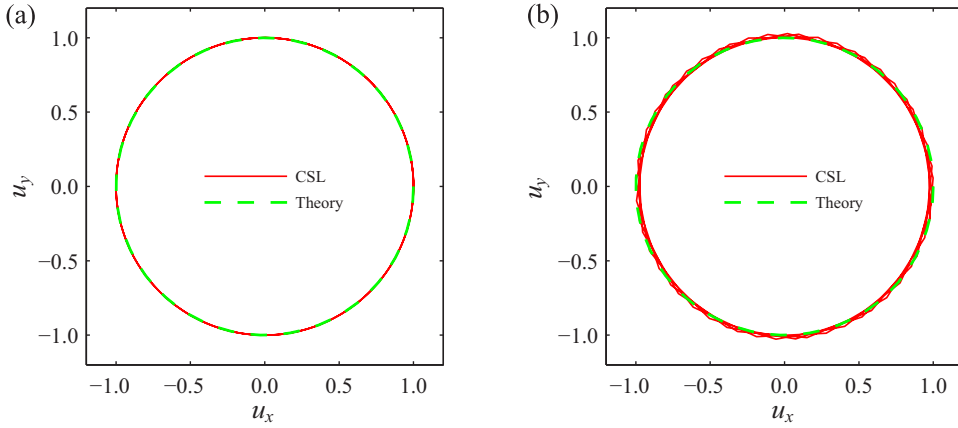
Fig. 2. Particle gyromotion: $N_{v_x} = 64, N_{v_y} = 64$. Particle mean velocity phase plot expressed in u_x against with u_y over four gyro-periods with CFL = 1 (a) and CFL = 15 (b).

Table 5
Streaming Weibel instability: $\Delta t = 0.5 \Delta x / v_{x_m}$, run to $t = 5$ and back to $t = 0$. The L^2 error and convergence order in space.

V	N = 16³		N = 32³		N = 64³		N = 128³	
	L^2 error	Order	L^2 error	Order	L^2 error	Order	L^2 error	Order
f	3.41E-01	—	7.33E-02	2.22	1.48E-02	2.30	2.07E-03	2.84
E_x	1.18E-04	—	3.97E-05	2.00	5.75E-06	2.79	6.85E-07	3.07
E_y	1.68E-05	—	3.56E-06	2.23	5.62E-07	2.66	7.31E-08	2.94
B_z	4.74E-07	—	1.04E-07	2.19	1.16E-08	3.16	1.36E-09	3.09

with the traditional explicit Eulerian scheme where the time step limited by the CFL condition. This advantage makes the proposed CSL to be more practical in lengthy simulation.

The above arguments indicate that the proposed CSL with general parametrized PP limiter has third order accuracy in space and two order accuracy in time, as well as conserves mass and preservers the positivity of the distribution function. It is worth noting that, with the parametrized PP limiter, it is straightforward to extend the proposed CSL to be a positivity-preserving scheme with general higher-order spatial accuracy.

4.3. Streaming weibel instability

So far, the CSL scheme for Vlasov equation and the IFEM solver for Maxwell equations have been validated independently. In this section, the Streaming Weibel instability (1d2v) is presented to investigate the performance, in terms of accuracy, conservation properties, and efficiency, of the proposed plasma solver CSL-IFEM for the complete VM system with the coupling of CSL and IFEM. Following [48,50,62], here we consider a reduced version of the VM equations,

$$\partial_t f + v_x \partial_x f - (E_x + v_y B_z) \partial_{v_x} f - (E_y - v_x B_z) \partial_{v_y} f = 0,$$
$$\partial_t E_x = -J_x, \quad \partial_t E_y = -c^2 \partial_x B_z - J_y, \quad \partial_t B_z = -\partial_x E_y,$$

where f is the electron distribution function with a neutralizing ion background. The initial conditions are given by

$$f(v_x, v_y, 0) = \frac{1}{2\pi\beta} \exp\left(-v_x^2/\beta\right)\left(\exp\left[(v_y - v_0)^2/\beta\right] + \exp\left[(v_y + v_0)^2/\beta\right]\right)$$

$$E_x(x, 0) = 0, E_y(x, 0) = 0, B_z(x, 0) = \alpha \sin(kx),$$

with $\alpha = 10^{-3}$, $\beta = 10^{-2}$, $v_0 = 0.3$ and $k = 0.2$.

In our simulations, we set the phase space to be $[0, L_x] \times [-v_{x_m}, v_{x_m}] \times [-v_{y_m}, v_{y_m}]$ with grids $N = N_x \times N_{v_x} \times N_{v_y}$ and $v_{x_m} = v_{y_m} = 1$. The speed of light $c = 1$. For convenience, we use a fixed time step Δt. The periodic boundary conditions are imposed both on Vlasov equation and Maxwell equations.

First, we investigate the spatial accuracy of the proposed CSL-IFEM. Table 5 summaries the L^2 error and convergence order in space with $\Delta t = 0.5 \Delta x / v_{x_m}$. Here the L^2 error is evaluated with Eq. (34), and the reference solution V_r is obtained from the well-known time reversibility of the VM system [48,50]. More specifically, with initial condition $f(x, v, 0)$, $E(x, 0)$ and $B(x, 0)$. one runs the code to obtain the numerical solution $f(x, v, t)$, $E(x, t)$ and $B(x, t)$ at specific time t. If one chooses the $f(x, -v, t)$, $E(x, t)$ and $-B(x, t)$ as the initial condition at time t, then the numerical solution at $2t$ theoretically should

Table 6

Streaming Weibel instability: $N = 80^3$, $t = 5$. The L^2 error and convergence order in time.

V	$\Delta t = 0.016$		$\Delta t = 0.032$		$\Delta t = 0.064$		$\Delta t = 0.128$	
	L^2 error	Order	L^2 error	Order	L^2 error	Order	L^2 error	Order
f	1.20E-09	–	5.68E-09	2.24	2.46E-08	2.11	1.04E-07	2.08
E_x	1.31E-06	–	5.27E-06	2.01	2.12E-05	2.01	8.63E-05	2.03
E_y	2.26E-06	–	9.09E-06	2.01	3.65E-05	2.01	1.47E-04	2.01
B_z	2.27E-06	–	9.14E-06	2.01	3.67E-05	2.01	1.48E-04	2.01
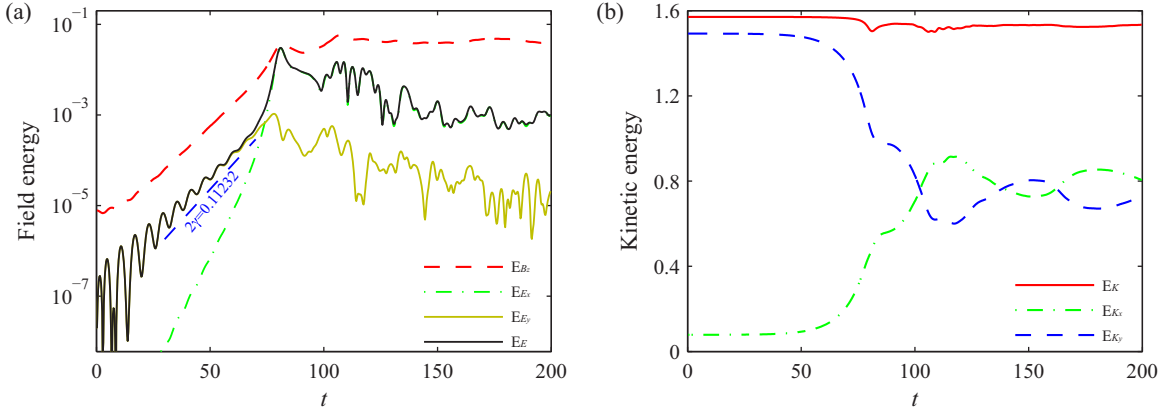
Fig. 3. Streaming Weibel instability: $N_x = 128, N_{v_x} = 128, N_{v_y} = 128, \Delta t = 0.25$. Time evolution of field energy (a) and kinetic energy (b).

recover $f(x, -v, 0)$, $\boldsymbol{E}(x, 0)$ and $-\boldsymbol{B}(x, 0)$. Here we run this problem up to $t = 5$ and back to $t = 0$, the expected third order accuracy for all variables is observed in Table 5. Then we test the temporal order accuracy of current CSL-IFEM. In Table 6, we present the temporal L^2 error and convergence order of CSL-IFEM with $N = 80^3$ up to $t = 5$. The L^2 error is obtained from Eq. (35), where the reference solution is obtained by using a small-time step ($\Delta t = 10^{-3}$). Similar with the numerical experiment in Section 4.2, here we chose $\hat{V} = \sqrt{\int |v_x f|^2 dx dv_x dv_y}$ for $V = f$ and $\hat{V} = \sqrt{\int |V|^2 dx}$ for $V = E_x, E_y$ or B_z. From Table 6, the expected second order in time is clearly observed.

To further verify the accuracy of our CSL-IFEM, in Fig. 3 we plot the time evolution of field energy and kinetic energy, where the electric energy $E_E = E_{E_x} + E_{E_y}$ with $E_{E_x} = \frac{1}{2} \int |E_x|^2 dx$ and $E_{E_y} = \frac{1}{2} \int |E_y|^2 dx$, the magnetic energy $E_{B_z} = \frac{1}{2} \int |B_z|^2 dx$, as well as the kinetic energy $E_K = E_{K_x} + E_{K_y}$ with $E_{K_x} = \frac{1}{2} \int f v_x^2 dx dv_x dv_y$ and $E_{K_y} = \frac{1}{2} \int f v_y^2 dx dv_x dv_y$. Both field energy in Fig. 3(a) and kinetic energy in Fig. 3(b) predicted by proposed CSL-IFEM using $N = 128^3$ and $\Delta t = 0.25$ agree well with the results of Cheng *et al.* [48]. (It should be noted the mean energy located at x_2 (y) direction is used in [48]). Although a large time step is used (nearly be ten times larger than the one used in [48]), the linear growth rate of magnetic B_z and inductive electric field E_x shown in Fig. 3(a) still agree well with the results of Califano *et al.* [62], which further demonstrates good performance of proposed CSL-IFEM.

Now let we investigate the performance of proposed CSL-IFEM on the conservation properties, in terms of system mass L_1, moment $\boldsymbol{P}$, and total energy E_t, where $L_1 = \int f dx dv_x dv_y$, $\boldsymbol{P} = \int \boldsymbol{v} f dx dv_x dv_y + \int \boldsymbol{E} \times \boldsymbol{B} dx$, and $E_t = E_K + E_E + E_{B_z}$. We further define the conservation error as $|\Delta V| = |V(t) - V(0)|$, where V represents for L_1, P_x, P_y, or E_t. In Fig. 4, we plot the time evolution of conservation error for proposed CSL-IFEM using the fine grids $N = 128^3$, and $\Delta t = 0.25$ together with the results by using the coarse grids $N = 32 \times 64 \times 64$ and $\Delta t = 0.25$. Thanks to the CSL scheme, the system mass L_1 is exactly conserved as expected. As for moment conservation, the proposed CSL-IFEM conserves P_x very well, but could not exactly conserve P_y, which is also observed in [48]. It also can be seen that the proposed CSL-IFEM could not exactly conserve the energy, but the error can be preserved rather small. Encouragingly, the similar conservation errors are also observed in Fig. 4(b), even using the coarse grids.

Besides the conservation properties, we are interested in the efficiency, here we expect the CSL-IFEM could provide reasonable physical results by using as large time step as possible. The results by using two different time step sizes $\Delta t = 0.6$ and $\Delta t = 0.06$ with same grids $N = 128^3$ are presented. To clearly show present CSL-IFEM could provide reasonable results with large CFL number for the complete VM system, in Fig. 5 we present the time evolution of the CFL number, where $CFL = \frac{\Delta t}{\min(\Delta x / v_{x_m}, \Delta v / |\boldsymbol{a}|_{\max})}$ with $\boldsymbol{a} = \boldsymbol{E} + \boldsymbol{v} \times \boldsymbol{B}$. It can be seen that the largest CFL number for fixed time step $\Delta t = 0.6$ and $\Delta t = 0.06$ are around 10 and 1 respectively. Fig. 6 presents the time evolution of macroscopic magnetic field B_z (Anti-symmetric respects to $x = L_x/2$) and microscopic velocity distribution function at $v_x = 0$ and $v_y = 0$. It can be seen that both macroscopic and microscopic structure captured by CSL-IFEM with $\Delta t = 0.6$ (CFL=10) can be comparable to the results with $\Delta t = 0.06$ (CFL=1), which demonstrates the high efficiency of proposed CSL-IFEM.
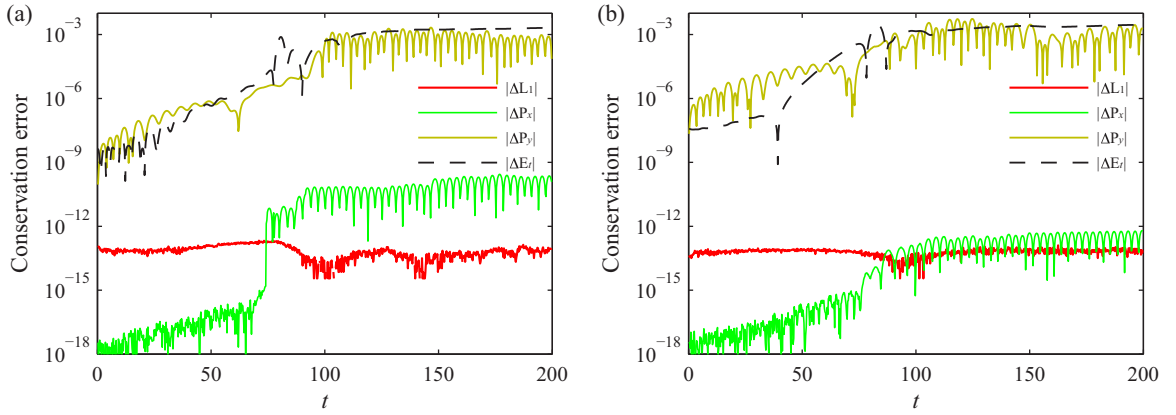
Fig. 4. Streaming Weibel instability: $\Delta t = 0.25$. Time evolution of conservation error with fine grids $N_x = 128, N_{v_x} = 128, N_{v_y} = 128$ (a) and coarse grids $N_x = 32, N_{v_x} = 64, N_{v_y} = 64$ (b).
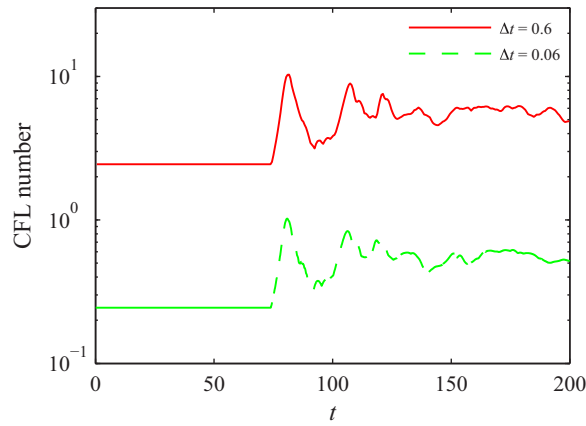

Fig. 5. Streaming Weibel instability: $N_x = 128, N_{v_x} = 128, N_{v_y} = 128$. Time evolution of CFL number with $\Delta t = 0.6$ and $\Delta t = 0.06$.
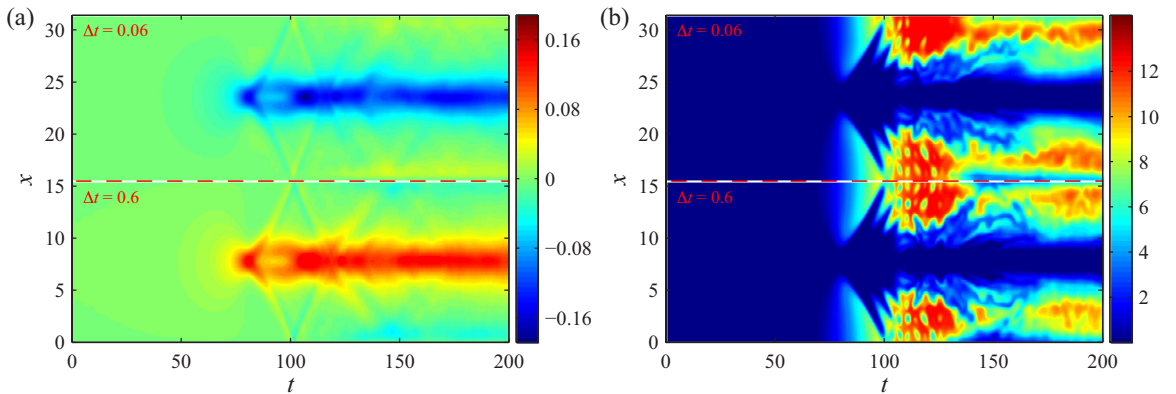
Fig. 6. Streaming Weibel instability: $N_x = 128, N_{v_x} = 128, N_{v_y} = 128$, with $\Delta t = 0.06$ (up) and $\Delta t = 0.6$ (bottom). Time evolution of magnetic field B_z (a) and velocity distribution function at $v_x = 0$ and $v_y = 0$ (b) against the physical space x.

The above arguments indicate that the proposed CSL-IFEM has third order accuracy in space and second order accuracy in time, as well as be free from the CFL restriction on phase transportation and speed of light. The numerical results also suggest that the proposed method exactly conserves the mass, but mimics the moment and energy conservation. The use of the CSL, IFEM and the appropriate coupling treatment makes the current method provide satisfactory solution even using a large time step.
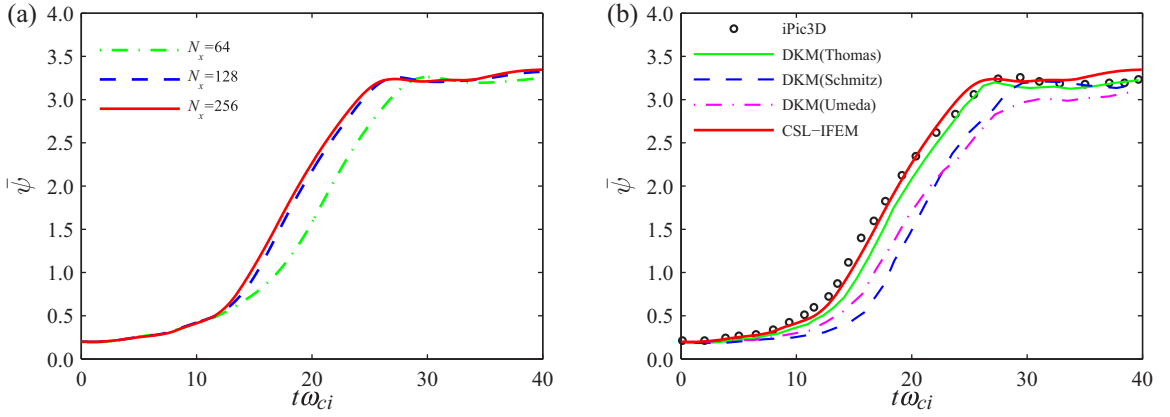
Fig. 7. Magnetic reconnection: $\Delta t = 1$. Time evolution of reconnected flux predicted by CSL-IFEM with different physical grids N_x(a); the reconnected flux of CSL-IFEM with $N_x = 256$, compared to the results of iPic3D[55], DKM(Thomas)[64], DKM(Schimtz)[38], and DKM(Umeda)[37](b).

4.4. Magnetic reconnection

In this section, we apply the CSL-IFEM to a 2d3v magnetic reconnection simulation, which represents a strong numerical challenge for direct kinetic solver because of the requirement of the huge memory and CPU time. This challenging multidimensional simulation is presented here to verify the accuracy, stability, and efficiency of the proposed CSL-IFEM. Both ions and electrons dynamic will be involved, which follows the VM system Eqs. (5) and (6), and we don't repeat it.

Here the Geospace Environmental Modelling (GEM) magnetic reconnection challenge as presented by Birn et al. [63] is used. The initial component of the magnetic corresponding to the Harris sheet equilibrium in the x-y plan reads,

$$B_x(y) = B_0 \tanh(y/\lambda_0),$$

where $\lambda_0 = \lambda_i/2$ is the half thickness of the current sheet, and $\lambda_i = c/\omega_{pi}$ is the ion inertial length, while the initial electric field $\boldsymbol{E}(x, y) = (E_x, E_y, E_z)$ is set to be zero. The initial electrons and ions follow a shifted Maxwellian distribution:

$$f_s^0 = \frac{n(y)}{\left(\sqrt{2\pi} v_{ts}\right)^3} \exp\left[-\frac{v_x^2 + v_y^2 + (v_z - v_{ds})^2}{2v_{ts}^2}\right] + \frac{n_b}{\left(\sqrt{2\pi} v_{ts}\right)^3} \exp\left[-\frac{v_x^2 + v_y^2 + v_z^2}{2v_{ts}^2}\right],$$

where the density is given by $n(y) = \frac{n_e}{\cosh^2(y/\lambda_0)}$ with background density $n_b = 0.2n_e$, and the drift velocity $v_{ds} = -\frac{2m_s v_{ts}^2}{q_s B_0 \lambda_0}$. Accordingly, the magnitude of the initial magnetic field reads

$$B_0 = \frac{1}{c}\sqrt{2\sum_s \left(w_{ps} v_{ts} m_s/q_s\right)^2}.$$

Similar with other kinetic simulations for GEM challenge [37,38,55,64], the temperature ration $T_i/T_e = 5$ and a reduced mass ratio $m_i/m_e = 25$ are used. The physical domain is set to be $[-L_x, L_x] \times [-L_y, L_y]$ with $L_x = 12.8\lambda_i$ and $L_y = 6.4\lambda_i$. Besides, an initial perturbation is added to the magnetic vector $\delta\boldsymbol{B} = \nabla\phi \times \boldsymbol{e}_z$ with $\phi(x, y) = \phi_0 \cos(\pi x/L_x) \cos(\pi y/2L_y)$, where $\phi_0 = 0.1B_0\lambda_i$.

In our simulation, the reference length, temperature, density, and mass are set to be $x_0 = \lambda$ (electron Debye length), $T_0 = T_e$, $n_0 = n_e$, and $m_0 = m_e$, respectively. Following normalized process in Section 2, one can obtain that the normalized light speed $c = 13.856$, ion inertial length $\lambda_i = 69.28$, and initial magnetic $B_0 = 0.25$. Besides, the normalized electron thermal velocity $v_{te} = 1$, ion thermal velocity $v_{ti} = \frac{v_{te}}{\sqrt{5}}$, electron drift velocity $v_{de} = 0.2309$, and ion drift velocity $v_{di} = -5v_{de}$. Accordingly, the ion mass $m_i = 25$, and ion cyclotron frequency $w_{ci} = qB_0/m_i = 0.01$. Because of the symmetry constraints, one quarter of the total system, i.e., $[0, L_x] \times [0, L_y]$, is simulated in present study. The conducting wall is imposed on $y = L_y$, while the symmetry conditions are imposed on other boundaries. The whole phase space is discretized with $N = N_x \times N_y \times N_{v_x} \times N_{v_y} \times N_{v_z}$, where the velocity space is set to be $[-8, 8]^3$ and $[-4, 4]^3$ for electrons and ions and discretized with $N_{v_x} \times N_{v_y} \times N_{v_z} = 26 \times 26 \times 26$ uniform grid points. For all simulations, the electrons and ions share the same phase space grids with $N_x = 2N_y$, and the fixed time step $\Delta t = 1$ is used. We run all the simulations up to $t = 4000$, i.e., $w_{ci}t = 40$.

The normalized reconnected flux $\bar{\psi} = \psi/(B_0\lambda_i)$ with $\psi = \int_0^{L_x} B_y(x, y = 0)dx$ is used to validate the proposed CSL-IFEM. Fig. 7 shows the time evolution of normalized reconnected flux with different physical grids N_x, together with the results of other kinetic solvers, including particle solver iPic3D [55] and several DKM solvers [37,38,64]. The grid convergence can be clearly seen in Fig. 7 (a), which demonstrates the stability of the CSL-IFEM. From Fig. 7 (b), one can observes that the reconnected flux predicted by the CSL-IFEM with $N_x = 256$ agrees well with the solutions of iPic3D and the other DKM solvers.
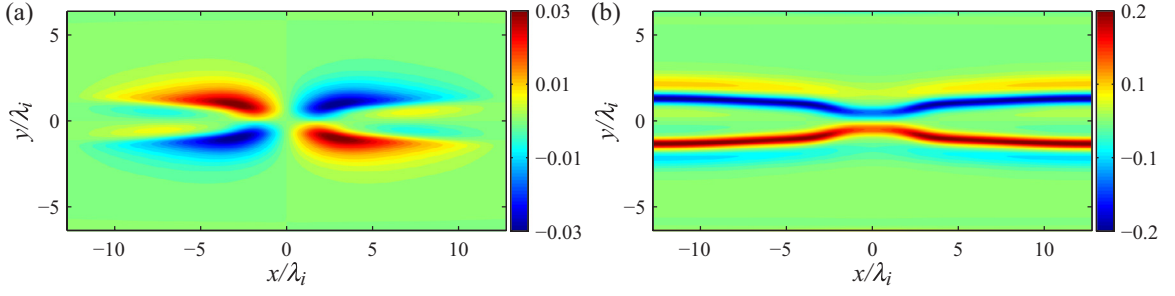
Fig. 8. Magnetic reconnection: $\Delta t = 1.0$, $N_x = 256$. The out-of-plane magnetic field B_z (a) and the Hall electric field E_y (b) at $\omega_{ci} t = 16$.
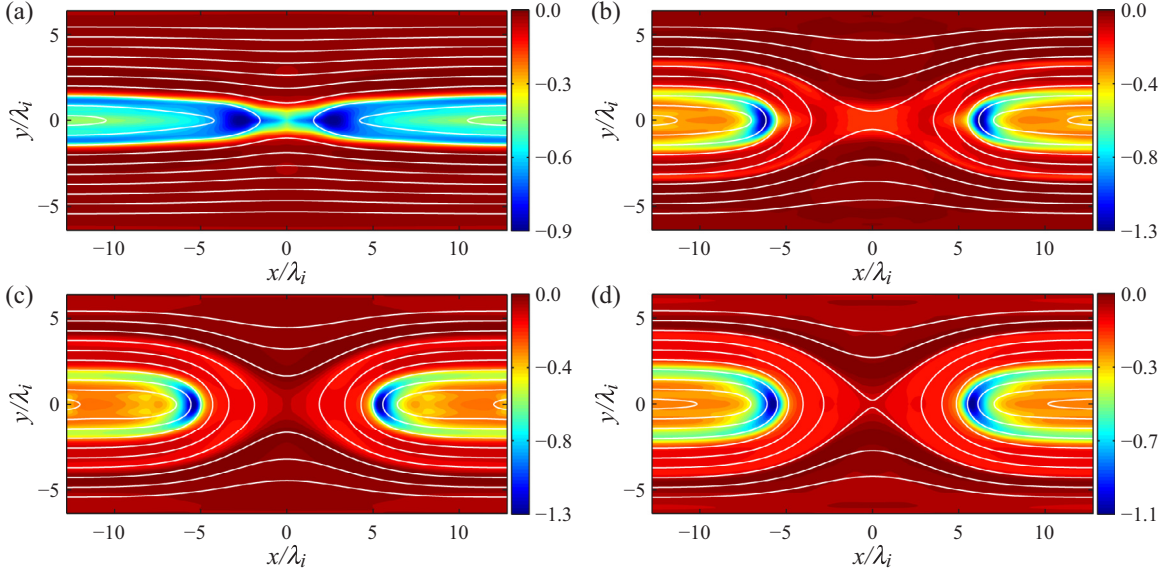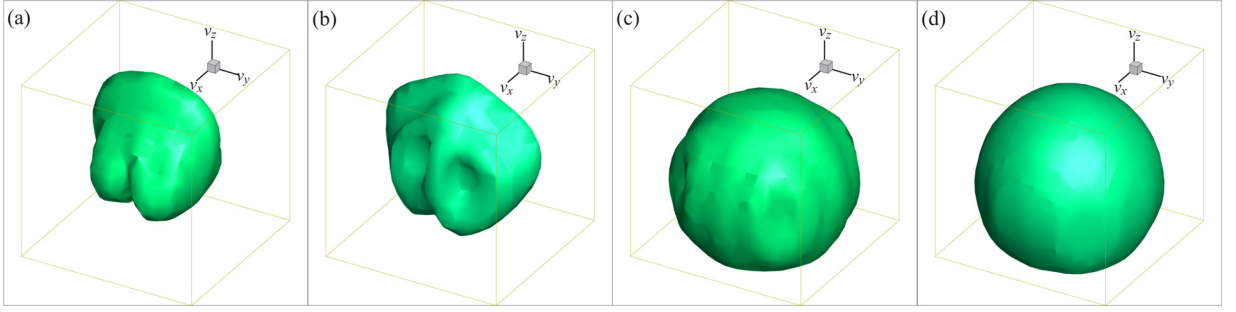

Fig. 9. Magnetic reconnection: $\Delta t = 1.0$, $N_x = 256$. Time evolution of magnetic field lines (white solid line) and the contours of out-of-plane current density J_z at $\omega_{ci} t = 16$ (a), $\omega_{ci} t = 24$ (b), $\omega_{ci} t = 32$ (c), and $\omega_{ci} t = 40$ (d).

It should be noted that even the large time step $\Delta t = 1$ (the CFL number is around 8 for $N_x = 256$) is used, the CSL-IFEM still provides satisfactory results, thanks to its high-order-accuracy. Using sparse matrix in IFEM, dimensional splitting in CSL, as well as the large time step makes the proposed CSL-IFEM practical in multidimensional simulations. The computational costs for three physical girds on the workstation [16 Intel(R) Xeon(R) Gold 6144 CPU @ 3.50GHz] by using 8 OpenMP threads are 2.4h, 11.1h and 42.8h respectively, which demonstrates the scaling of present CSL-IFEM. Previous research works [55,63] show that the difference in the ion and electron dynamics give rise to Hall currents and then produce an out-of-plane magnetic field with quadrupolar structure, which plays a key role in the magnetic reconnection. Without this Hall current, the reconnection rate will be drastically reduced. Encouragingly, the quadrupolar structure of the out-of-plane magnetic field B_z is reproduced by proposed CSL-IFEM, as shown in Fig. 8 (a). In Fig. 8 (b), the Hall electric field E_y is also presented, which marks the magnetic separatrices.

Fig. 9 presents the time evolution of the magnetic lines and the contours of the out-of-plane current density J_z. Given the similar structure at the early stage, here we only present the current density and magnetic lines after $\omega_{ci} t = 16$, which corresponds to normalized reconnected flux $\tilde{\psi} = 1$ shown in Fig. 7. At the time $\omega_{ci} t = 16$, the central current density tends to separate and the separatrix in the magnetic topology can be seen. Then the current density rearranges itself in the diffusion region and the reconnections starts rapidly. The separatrix and X-point in the magnetic topology can be seen at $\omega_{ci} t = 24$, these features are more obvious at $\omega_{ci} t = 32$ and $\omega_{ci} t = 40$. Fig. 9 also shows a common behavior of the current density in the vicinity of an active X point: a reduced current density concentrated in a thin current sheet is formed in the diffusion region, while a strongly enhanced current density is formed in the adjacent region. These observations are in agreement with other kinetic simulations [55,63].

To further verify the capability of present CSL-IFEM, in Fig. 10 we present the electrons distribution function f at the X point ($x=0$, $y=0$). Due to the same reason with Fig. 9, we only present the results after $\omega_{ci} t = 16$. From Fig. 10 (a) and (b), the strong non-equilibrium effect can be clearly seen, which indicates that the kinetic methods are necessary, at least in

Fig. 10. Magnetic reconnection: $\Delta t = 1.0$, $N_x = 256$. Time evolution of distribution function $f_e(v_x, v_y, v_z)$ of electrons for $x = 0, y = 0$ at $\omega_{ci}t = 16$ (a), $\omega_{ci}t = 24$ (b), $\omega_{ci}t = 32$ (c), and $\omega_{ci}t = 40$ (d). The velocity box ranges from [-4.8,4.8] for v_x and v_y and [-2.88,6.72] for v_z.
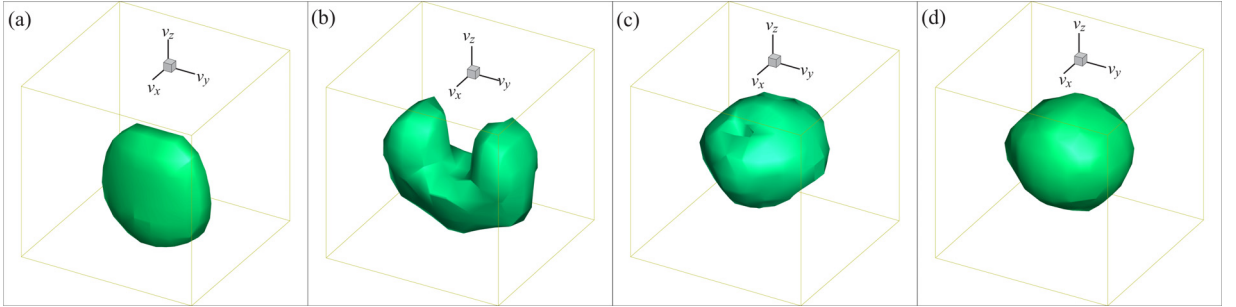
Fig. 11. Magnetic reconnection: $\Delta t = 1.0$, $N_x = 256$. Time evolution of distribution function $f_i(v_x, v_y, v_z)$ of ions for $x = 0, y = 0$ at $\omega_{ci}t = 16$ (a), $\omega_{ci}t = 24$ (b), $\omega_{ci}t = 32$ (c), and $\omega_{ci}t = 40$ (d). The velocity box ranges from [-1.44,1.44] for v_x, v_y and v_z.

diffusion region, if the accurate magnetic reconnection is expected. After $\omega_{ci}t = 32$, the distribution function tends to reach equilibrium state, which might be due to the saturation of reconnection. Similar observation can be seen in the evolution of ions distribution function shown in Fig. 11, but the ions tend to be more ordered.

The above arguments indicate that the proposed CSL-IFEM still has nice performance on accuracy, stability and efficiency in challenging multidimensional simulation.

5. Conclusions

In this paper, bridging a conservative semi-Lagrangian scheme (CSL) for Vlasov equation and an implicit finite element method (IFEM) for Maxwell equations with the general Ohm law, we develop a stable, accurate and efficient direct kinetic solver, termed CSL-IFEM, for the Vlasov Maxwell system. The proposed CSL-IFEM has third-order accuracy in space and second-order accuracy in time, as well as being free from the CFL limitation which is favorable in long time simulations. The accuracy and efficiency (being free from CFL limitation) of IFEM and CSL are confirmed by benchmarks for the 2d electromagnetic wave and 2v particle gyromotion independently, and the accuracy and efficiency of CSL-IFEM is verified by a 1d2v streaming Weibel instability simulation. The Weibel instability simulation also proves that the proposed method conserves the system mass, while mimics the moment and energy conservation. The nice performance, in terms of accuracy, stability and efficiency of proposed CSL-IFEM is further demonstrated by a 2d3v magnetic reconnection simulation. Numerical results demonstrate that the proposed CSL-IFEM is a stable and reliable method for the multidimensional Vlasov Maxwell system.

The proposed CSL-IFEM is free from the CFL limitation, but it still involves a stability restriction: the time step should be less than the plasma period due to the explicit coupling of Vlasov solver and Maxwell solver. The implicit or semi-implicit method is desired to alleviate this limitation, which will be considered in our future work. Additionally, considering more realistic problems in 3d3v dimensions, massive parallelization and memory reduction technique should be required. A more efficient parallelization of CSL-IFEM is expected and seems to be practical, due to the use of dimensional splitting technique in the Vlasov equation. On the other hand, for 3d3v simulations, a large number of discrete velocities may be required to capture the correct distribution function, where the memory requirement and computational cost will be demanding. Thus, developing memory reduction techniques is crucial for the direct kinetic solver, especially the flows involving a large wide range of velocities. The adaptive grids, sparse technology, or dynamic low-rank approximations might be used to reduce the memory and will constitute further research.

Declaration of Competing Interest

CRediT authorship contribution statement

Hongtao Liu: Conceptualization, Methodology, Software, Validation, Writing - original draft. **Xiaofeng Cai:** Methodology, Validation, Writing - review & editing. **Giovanni Lapenta:** Supervision, Resources, Writing - review & editing, Funding acquisition. **Yong Cao:** Supervision, Project administration, Validation, Funding acquisition.

Acknowledgment

References

[1] Chen FF. Introduction to plasma physics and controlled fusion, vol 1. Springer; 1984. doi:101007/978-1-4757-5595-4.

[2] Barber RW, Emerson DR. Challenges in modeling gas-phase flow in microchannels: from slip to transition. Heat Transfer Eng 2006;27(4):3–12. doi:10.1080/01457630500522271.

[3] Birdsall CK, Langdon AB. Plasma physics via computer simulation. Taylor & Francis; 2004. doi:101201/9781315275048.

[4] Markidis S, Lapenta G, et al. Multi-scale simulations of plasma with iPIC3D. Math Comput Simulat 2010;80(7):1509–19. doi:10.1016/j.matcom.2009.08.038.

[5] Lapenta G. Particle simulations of space weather. J Comput Phys 2012;231(3):795–821. doi:10.1016/j.jcp.2011.03.035.

[6] Lapenta G. Exactly energy conserving semi-implicit particle in cell formulation. J Comput Phys 2017;334:349–66. doi:10.1016/j.jcp.2017.01.002.

[7] Cao H, Cao Y, Chu Y, He X, Lin T. A huygens immersed-finite-element particle-in-cell method for modeling plasma-surface interactions with moving interface. Commun Nonlinear Sci Numer Simul 2018;59:132–48. doi:10.1016/j.cnsns.2017.10.015.

[8] Hu Y, Wang J. Expansion of a collisionless hypersonic plasma plume into a vacuum. Phys Rev E 2018;98(2):023204. doi:10.1103/PhysRevE.98.023204.

[9] Lapenta G, Jiang W. Implicit temporal discretization and exact energy conservation for particle methods applied to the poisson–boltzmann equation. Plasma 2018;1(2):242–58. doi:10.3390/plasma1020021.

[10] Camporeale E, Delzanno GL, Bergen BK, Moulton JD. On the velocity space discretization for the Vlasov–Poisson system: comparison between implicit hermite spectral and particle-in-Cell methods. Comput Phys Commun 2016;198:47–58. doi:10.1016/j.cpc.2015.09.002.

[11] Liu H, Quan L, Chen Q, Zhou S, Cao Y. Discrete unified gas kinetic scheme for electrostatic plasma and its comparison with the particle-in-cell method. Phys Rev E 2020;101(4):043307. doi:10.1103/PhysRevE.101.043307.

[12] Xu K, Huang J-C. A unified gas-kinetic scheme for continuum and rarefied flows. J Comput Phys 2010;229(20):7747–64. doi:10.1016/j.jcp.2010.06.032.

[13] Guo Z, Xu K, Wang R. Discrete unified gas kinetic scheme for all Knudsen number flows: low-speed isothermal case. Phys Rev E 2013;88(3):033305. doi:10.1103/PhysRevE.88.033305.

[14] Liu H, Cao Y, Chen Q, Kong M, Zheng L. A conserved discrete unified gas kinetic scheme for microchannel gas flows in all flow regimes. Comput Fluids 2018;167:313–23. doi:10.1016/j.compfluid.2018.03.023.

[15] Chen J, Liu S, Wang Y, Zhong C. Conserved discrete unified gas-kinetic scheme with unstructured discrete velocity space. Phys Rev E 2019;100(4):043305. doi:10.1103/PhysRevE.100.043305.

[16] Chen T, Wen X, Wang L-P, Guo Z, Wang J, Chen S. Simulation of three-dimensional compressible decaying isotropic turbulence using a redesigned discrete unified gas kinetic scheme. Phys Fluids 2020;32(12):125104. doi:10.1063/5.0029424.

[17] Yang LM, Zhao X, Shu C, Du YJ. Parametric reduced order modeling-based discrete velocity method for simulation of steady rarefied flows. J Comput Phys 2020:110037. doi:10.1016/j.jcp.2020.110037.

[18] Whealton JH, McGaffey RW, Meszaros PS. A finite difference 3-D Poisson-Vlasov algorithm for ions extracted from a plasma. J Comput Phys 1986;63(1):20–32. doi:10.1016/0021-9991(86)90082-3.

[19] Xiong T, Qiu J-M, Xu Z, Christlieb A. High order maximum principle preserving semi-Lagrangian finite difference WENO schemes for the vlasov equation. J Comput Phys 2014;273:618–39. doi:10.1016/j.jcp.2013.06.026.

[20] Cho SY, Boscarino S, Russo G, Yun S-B. Conservative semi-lagrangian schemes for kinetic equations part II: applications. J Comput Phys 2021:110281. doi:10.1016/j.jcp.2021.110281.

[21] Heath RE, Gamba IM, Morrison PJ, Michler C. A discontinuous Galerkin method for the Vlasov–Poisson system. J Comput Phys 2012;231(4):1140–74. doi:10.1016/j.jcp.2011.09.020.

[22] Rossmanith JA, Seal DC. A positivity-preserving high-order semi-Lagrangian discontinuous Galerkin scheme for the Vlasov–Poisson equations. J Comput Phys 2011;230(16):6203–32. doi:10.1016/j.jcp.2011.04.018.

[23] Qiu J-M, Shu C-W. Positivity preserving semi-Lagrangian discontinuous Galerkin formulation: theoretical analysis and application to the vlasov–Poisson system. J Comput Phys 2011;230(23):8386–409. doi:10.1016/j.jcp.2011.07.018.

[24] Filbet F, Sonnendrücker E, Bertrand P. Conservative numerical schemes for the Vlasov equation. J Comput Phys 2001;172(1):166–87. doi:10.1006/jcph.2001.6818.

[25] Banks JW, Hittinger JAF. A new class of nonlinear finite-volume methods for Vlasov simulation. IEEE T Plasma Sci 2010;38(9):2198–207. doi:10.1109/TPS.2010.2056937.

[26] Qiu J-M, Christlieb A. A conservative high order semi-Lagrangian WENO method for the Vlasov equation. J Comput Phys 2010;229(4):1130–49. doi:10.1016/j.jcp.2009.10.016.

[27] Liu C, Xu K. A unified gas kinetic scheme for continuum and rarefied flows V: multiscale and multi-component plasma transport. Commun Comput Phys 2017;22(5):1175–223. doi:10.4208/cicp.OA-2017-0102.

[28] Liu H, Shi F, Wan J, He X, Cao Y. Discrete unified gas kinetic scheme for a reformulated BGK-Vlasov-Poisson system in all electrostatic plasma regimes. Comput Phys Commun 2020:107400. doi:10.1016/j.cpc.2020.107400.

[29] Schumer JW, Holloway JP. Vlasov simulations using velocity-scaled hermite representations. J Comput Phys 1998;144(2):626–61. doi:10.1006/jcph.1998.5925.

[30] Le Bourdiec S, De Vuyst F, Jacquet L. Numerical solution of the Vlasov–Poisson system using generalized Hermite functions. Comput Phys Commun 2006;175(8):528–44. doi:10.1016/j.cpc.2006.07.004.
[31] Arber TD, Vann R. A critical comparison of Eulerian-grid-based Vlasov solvers. J Comput Phys 2002;180(1):339–57. doi:10.1006/jcph.2002.7098.
[32] Filbet F, Sonnendrücker E. Comparison of Eulerian Vlasov solvers. Comput Phys Commun 2003;150(3):247–66. doi:10.1016/S0010-4655(02)00694-X.
[33] Dimarco G, Pareschi L. Numerical methods for kinetic equations. Acta Numerica 2014:369–520. doi:10.1017/S0962492914000063.
[34] Qiu J-M, Shu C-W. Conservative semi-Lagrangian finite difference WENO formulations with applications to the Vlasov equation. Commun Comput Phys 2011;10(4):979–1000. doi:10.4208/cicp.180210.251110a.
[35] Liu H, Kong M, Chen Q, Zheng L, Cao Y. Coupled discrete unified gas kinetic scheme for the thermal compressible flows in all Knudsen number regimes. Phys Rev E 2018;98(5):053310. doi:10.1103/PhysRevE.98.053310.
[36] Einkemmer L. A performance comparison of semi-Lagrangian discontinuous Galerkin and spline based Vlasov solvers in four dimensions. J Comput Phys 2019;376:937–51. doi:10.1016/j.jcp.2018.10.012.
[37] Umeda T, Togano K, Ogino T. Two-dimensional full-electromagnetic Vlasov code with conservative scheme and its application to magnetic reconnection. Comput Phys Commun 2009;180(3):365–74. doi:10.1016/j.cpc.2008.11.001.
[38] Schmitz H, Grauer R. Kinetic Vlasov simulations of collisionless magnetic reconnection. Phys plasmas 2006;13(9):092309. doi:10.1063/1.2347101.
[39] Kormann K, Reuter K, Rampp M. A massively parallel semi-Lagrangian solver for the six-dimensional Vlasov–Poisson equation. Int J High Perform C 2019;33(5):924–47. doi:10.1177/1094342019834644.
[40] Crouseilles N, Glanc P, Hirstoaga SA, Madaule E, Mehrenberger M, Pétri J. A new fully two-dimensional conservative semi-Lagrangian method: applications on polar grids, from diocotron instability to ITG turbulence. Eur Phys J D 2014;68(9):1–10. doi:10.1140/epjd/e2014-50180-9.
[41] Cai X, Guo W, Qiu J-M. A high order semi-Lagrangian discontinuous galerkin method for Vlasov–Poisson simulations without operator splitting. J Comput Phys 2018;354:529–51. doi:10.1016/j.jcp.2017.10.048.
[42] Cai X, Guo W, Qiu J-M. A high order semi-Lagrangian discontinuous Galerkin method for the two-dimensional incompressible Euler equations and the guiding center vlasov model without operator splitting. J Sci Comput 2019;79(2):1111–34. doi:10.1007/s10915-018-0889-1.
[43] Pezzi O, Cozzani G, Califano F, Valentini F, Guarrasi M, Camporeale E, et al. ViDA: a vlasov–DArwin solver for plasma physics at electron scales. J Plasma Phys 2019;85(5). doi:10.1017/S0022377819000631.
[44] Kraus M, Kormann K, Morrison PJ, Sonnendrücker E. Gempic: geometric electromagnetic particle-in-cell methods. J Plasma Phys 2017;83(4). doi:10.1017/S002237781700040X.
[45] Sircombe NJ, Arber TD. Valis: a split-conservative scheme for the relativistic 2D Vlasov–Maxwell system. J Comput Phys 2009;228(13):4773–88. doi:10.1016/j.jcp.2009.03.029.
[46] Crouseilles N, Navaro P, Sonnendrücker E. Charge-conserving grid based methods for the vlasov–Maxwell equations. Comptes Rendus Mécanique 2014;342(10–11):636–46. doi:10.1016/j.crme.2014.06.012.
[47] Crouseilles N, Einkemmer L, Faou E. Hamiltonian splitting for the Vlasov–Maxwell equations. J Comput Phys 2015;283:224–40. doi:10.1016/j.jcp.2014.11.029.
[48] Cheng Y, Gamba IM, Li F, Morrison PJ. Discontinuous Galerkin methods for the Vlasov–Maxwell equations. SIAM J Num Anal 2014;52(2):1017–49. doi:10.1137/130915091.
[49] Juno J, Hakim A, TenBarge J, Shi E, Dorland W. Discontinuous Galerkin algorithms for fully kinetic plasmas. J Comput Phys 2018;353:110–47. doi:10.1016/j.jcp.2017.10.009.
[50] Cheng Y, Christlieb AJ, Zhong X. Energy-conserving discontinuous Galerkin methods for the Vlasov–Maxwell system. J Comput Phys 2014;279:145–73. doi:10.1016/j.jcp.2014.08.041.
[51] Munz C-D, Omnes P, Schneider R, Sonnendrücker E, Voss U. Divergence correction techniques for Maxwell solvers based on a hyperbolic model. J Comput Phys 2000;161(2):484–511. doi:10.1006/jcph.2000.6507.
[52] Pinto MC, Mounier M, Sonnendrücker E. Handling the divergence constraints in maxwell and vlasov–Maxwell simulations. Appl Math Comput 2016;272:403–19. doi:10.1016/j.amc.2015.07.089.
[53] Einkemmer L, Ostermann A, Piazzola C. A low-rank projector-splitting integrator for the Vlasov–Maxwell equations with divergence correction. J Comput Phys 2020;403:109063. doi:10.1016/j.jcp.2019.109063.
[54] Schmitz H, Grauer R. Comparison of time splitting and backsubstitution methods for integrating Vlasov's equation with magnetic fields. Comput Phys Commun 2006;175(2):86–92. doi:10.1016/j.cpc.2006.02.007.
[55] Ricci P, Lapenta G, Brackbill JU. A simplified implicit Maxwell solver. J Comput Phys 2002;183(1):117–41. doi:10.1006/jcph.2002.7170.
[56] Chen Y, Tóth G. Gauss's law satisfying energy-conserving semi-implicit particle-in-cell method. J Comput Phys 2019;386:632–52. doi:10.1016/j.jcp.2019.02.032.
[57] Zhang G-D, He X, Yang X. A decoupled, linear and unconditionally energy stable scheme with finite element discretizations for magneto-hydrodynamic equations. J Sci Comput 2019;81(3):1678–711. doi:10.1007/s10915-019-01059-1.
[58] Bai J, Cao Y, He X, Liu H, Yang X. Modeling and an immersed finite element method for an interface wave equation. Comput Math with Appl 2018;76(7):1625–38. doi:10.1016/j.camwa.2018.07.015.
[59] Saad Y. Iterative methods for sparse linear systems. SIAM; 2003.
[60] Sármány D, Botchev MA, van der Vegt JJW. Time-integration methods for finite element discretisations of the second-order Maxwell equation. Comput Math with Appl 2013;65(3):528–43. doi:10.1016/j.camwa.2012.05.023.
[61] Degond P, Deluzet F, Doyen D. Asymptotic-preserving particle-in-cell methods for the Vlasov–Maxwell system in the quasi-neutral limit. J Comput Phys 2017;330:467–92. doi:10.1016/j.jcp.2016.11.018.
[62] Califano F, Pegoraro F, Bulanov SV, Mangeney A. Kinetic saturation of the Weibel instability in a collisionless plasma. Phys Rev E 1998;57(6):7048. doi:10.1103/PhysRevE.57.7048.
[63] Birn J, Drake JF, Shay MA, Rogers BN, Denton RE, Hesse M, et al. Geospace environmental modeling (GEM) magnetic reconnection challenge. J Geophys Res 2001;106(A3):3715–19. doi:10.1029/1999JA900449.
[64] Trost TA. Coupling of vlasov-and fluid-codes with adaptive domain decomposition using the example of magnetic reconnection. Ruhr-Universität Bochum; 2017. Ph.D. thesis. URL https://hss-opus.ub.rub.de/opus4/frontdoor/index/index/docId/5156.